Microbial utilization of rare earth elements at cold seeps related to aerobic methane oxidation

Germain Bayon, Nolwenn Lemaitre, Jean-Alix J-A Barrat, Xudong Wang, Dong Feng, Sébastien Duperron

▶ **To cite this version:**

Germain Bayon, Nolwenn Lemaitre, Jean-Alix J-A Barrat, Xudong Wang, Dong Feng, et al.. Microbial utilization of rare earth elements at cold seeps related to aerobic methane oxidation. Chemical Geology, 2020, 555, pp.119832 -. 10.1016/j.chemgeo.2020.119832 . hal-03492528

HAL Id: hal-03492528
https://hal.science/hal-03492528v1

Submitted on 30 Aug 2022

HAL is a multi-disciplinary open access archive for the deposit and dissemination of scientific research documents, whether they are published or not. The documents may come from teaching and research institutions in France or abroad, or from public or private research centers.

L'archive ouverte pluridisciplinaire **HAL**, est destinée au dépôt et à la diffusion de documents scientifiques de niveau recherche, publiés ou non, émanant des établissements d'enseignement et de recherche français ou étrangers, des laboratoires publics ou privés.

Distributed under a Creative Commons Attribution - NonCommercial 4.0 International License

Version of Record: https://www.sciencedirect.com/science/article/pii/S0009254120303715
Manuscript_686c4c2b1955bf4429dcf204fb0b1324

Microbial utilization of rare earth elements at cold seeps related to aerobic methane oxidation

Germain Bayon[a]*, Nolwenn Lemaitre[b], Jean-Alix Barrat[c],

Xudong Wang[a,d], Dong Feng[d], Sébastien Duperron[e,f]

[a] IFREMER, Marine Geosciences Unit, 29280 Plouzané, France

[b] Institute of Geochemistry and Petrology, Department of Earth Sciences, ETH Zurich, CH-8092 Zurich, Switzerland

[c] Laboratoire Géosciences Océan, Université de Bretagne Occidentale et Institut Universitaire Européen de la Mer, 29280 Plouzané, France

[d] Shanghai Engineering Research Center of Hadal Science and Technology, College of Marine Sciences, Shanghai Ocean University, Shanghai 201306, China

[e] Muséum national d'Histoire naturelle–UMR7245 (MNHN CNRS) Mécanismes de Communication et Adaptation des Micro-organismes (MCAM), 75005 Paris, France

[f] Institut Universitaire de France, Paris, France

Total word count: 5,771

* corresponding author: gbayon@ifremer.fr

phone: 00 33-2-98-22-44-54

© 2020 published by Elsevier. This manuscript is made available under the CC BY NC user license
https://creativecommons.org/licenses/by-nc/4.0/

Abstract

A major breakthrough in the field of rare earth element (REE) geochemistry has been the recent discovery of their utility to microbial life, as essential metalloenzymes catalysing the oxidation of methanol to formaldehyde. Lanthanide-dependent bacteria are thought to be ubiquitous in marine and terrestrial environments, but direct field evidence of preferential microbial utilization of REE in natural systems is still lacking. In this study, we report on the REE and trace element composition of the tube of a siboglinid worm collected at a methane seep in the Gulf of Guinea; a tube-dwelling annelid that thrives in deep-sea chemosynthetic ecosystems. High-resolution trace element profiles along the chitin tube indicate marked enrichments of lanthanum (La) and cerium (Ce) in its oxic part, resulting in REE distribution patterns that depart significantly from the ambient seawater signature. Combined with various geochemical and microbiological evidence, this observation provides direct support for an active consumption of light-REE at cold seeps, associated with the aerobic microbial oxidation of methane. To further evaluate this hypothesis, we also re-examine the available set of REE data for modern seep carbonates worldwide. While most carbonate concretions at cold seeps generally display REE distribution patterns very similar to those for reduced pore waters in marine sediments, we find that seafloor carbonate pavements composed of aragonite commonly exhibit pronounced light-REE enrichments, as inferred from high shale-normalized La/Gd ratio (> ~ 0.8), interpreted here as possibly reflecting the signature of lanthanide-dependent methanotrophic activity. This finding opens new perspectives for revisiting REE systematics in ancient seep carbonates and other microbialites throughout the Earth's history. In particular, the geochemical imprint of aerobic methane oxidation could be possibly traced using REE in Archaean stromatolites and other archives of Precambrian seawater chemistry, potentially providing new insights into the oxygenation of early Earth's oceans and associated microbiogeochemical processes.

Keywords: tubeworms; Siboglinidae; Lanthanide-dependent bacteria; metalloenzymes; methylotrophy; Regab; authigenic carbonates; Archaean

1. Introduction

Trace elements have long been known for their utility to biological systems, playing key roles in metalloenzymes that mediate important biochemical reactions (*e.g.*, Bowen, 1966). To some extent, the lanthanides, or rare earth elements (REE), also share biologically relevant properties (Tyler, 2004). For instance, they are thought to stimulate plant growth when added as fertilisers in agriculture (Tyler, 2004). However, compared to iron and other well-known essential metals, the biological role of REE still remains largely unexplored and poorly understood (Skrovan and Martinez-Gomez, 2015). A few years ago, a series of experimental works showed that microorganisms involved in the aerobic oxidation of methane were strongly dependent upon REE availability (*e.g.*, Fitriyanto et al., 2011; Nakagawa et al., 2012; Pol et al., 2014), demonstrating that light-REE (LREE), especially lanthanum (La) and cerium (Ce), were playing an active role as cofactors in a particular type (XoxF) of methanol dehydrogenase; a quinoprotein that catalyses the conversion of methanol to formaldehyde. Importantly, follow-up studies revealed that REE-dependent bacteria were probably ubiquitous in both marine and terrestrial environments (Taubert et al., 2015; Ochsner et al., 2019; Picone and Op den Camp, 2019). In a study that investigated the massive gas plume released to the Gulf of Mexico during the *Deepwater Horizon* blowout, Shiller et al. (2017) even proposed that aerobic methanotrophy could play a previously unrecognized role in the marine geochemical cycle of the REE, acting as a net sink for dissolved LREE in seawater. More recently, in a companion paper, we have reported the first documented evidence for methanotrophy-driven La enrichments in cold seep mussels from the South China Sea, both in the carbonate shells and associated soft tissues (Wang et al., 2020). A major finding of that work was the discovery that thiotrophic bivalves from the same sites (i.e. associated with sulphur-oxidizing bacteria) did not display any particular LREE enrichments, hence clearly suggesting that their occurrence in chemosynthetic mussels was solely related to lanthanide-

dependent methanotrophy. To date, this latter study represents the only field evidence for preferential REE utilization during methane oxidation processes in the marine environment. Additional work is needed to clarify the mechanism by which REE may be consumed by microbial activity in methane-rich environments, but also to assess whether authigenic carbonates and other geological archives of past fluid seepage may provide a record for REE-dependent methanotrophy.

Siboglinid tubeworms are ubiquitous chemosynthetic organisms at deep-sea hydrocarbon seeps and hydrocarbon vents (*e.g.*, Sibuet and Olu, 1998; Bright and Lallier, 2010), where they form large colonies (or 'bushes') at the seafloor, growing on hard substrates (Fig. 1a). For nutrition, siboglinid annelids rely entirely on internal suphide-oxidizing bacterial symbionts, which are hosted within specialized cells in a specific organ called the trophosome (*e.g.*, Boetius, 2005). At seeps, the required supply of sulphide comes from the underlying anoxic sediment (via anaerobic oxidation of methane or AOM; $CH_4 + SO_4^{2-} \rightarrow HCO_3^- + HS^- + H_2O$), where the posterior extension of the tube is rooted, often anchored into carbonates, but also, to a lesser extent, from the anterior fraction of the tube, thanks to in-tube water circulation (Julian et al., 1999; Cordes et al., 2005). In contrast, oxygen is acquired exclusively from overlying bottom waters at the anterior end of the animal via a large branchial plume (*e.g.*, Freytag et al., 2001). Siboglinid tubes also act as a direct conduit for seawater sulphate down to the buried posterior extension within the anoxic sediment (*e.g.*, Cordes et al., 2005). This process further promotes AOM and subsequent *in situ* production of dissolved sulphide that can be used as an additional source of energy for the internal symbionts. Within the animal, both dissolved sulphide and oxygen are co-transported by a specialized haemoglobin through the circulatory system to the trophosome (Flores et al., 2005). Siboglinid tubes are composed of chitin crystallites embedded in a protein matrix

(Gaill et al., 1992), but also host abundant and diverse microbial communities, including aerobic methane-oxidizing bacteria (Duperron et al., 2009; Medina-Silva et al., 2018). As such, the chitin-rich tube of siboglinid worms represents an ideal archive for investigating the links between trace elements and microbial activity at methane seeps and, in particular, to test the hypothesis that aerobic oxidation of methane can result in the preferential microbial utilization of light-REE.

In this study, we report REE and other trace element abundances along the tube of one specimen of *Escarpia southwardae*; a tubeworm from the annelid family Siboglinidae that is encountered in West African cold seeps (Andersen et al., 2004). This study builds upon an earlier investigation of the same tubeworm, which combined the characterization of the bacterial symbionts together with preliminary geochemical analyses (Mn, Fe, Sr, Zr) of the chitin tube (Duperron et al., 2014). The new REE data reported here are found to display major fluctuations along the tube, reflecting the combination of various factors, such as the presence of detrital particles embedded within the tube matrix, changes in the relative contribution of anoxic pore water versus oxic seawater, but also, importantly, the preferential utilization of La and other light-REE due to the aerobic oxidation of methane.

2. Material and methods

2.1. Study area and sample preparation

The studied siboglinid tube was collected by remotely operated vehicle (ROV) at the Regab cold seep using a hydraulically actuated Bushmaster device (5.798°S, 9.711°E; 3152 m water depth; Fig. 1a). Regab is a ~800 m wide giant pockmark at the Western African margin, characterized by intense methane seepage and the occurrence of gas hydrates,

massive carbonate deposits, and abundant chemosynthetic communities at the seafloor (*e.g.*, Charlou et al., 2004; Ondréas et al., 2005; Olu-Leroy et al., 2007; Pop Ristova et al., 2012; Marcon et al., 2014; Lemaitre et al., 2014). Upon recovery, the ~1-m-long chitinous tube was cut in sections perpendicular to the length of the tube, with sections S1 and S55 corresponding to the most anterior and posterior parts of the tube, respectively (Fig. 1b). All tube samples were cleaned with ultrapure water in ultrasonic bath prior to being digested with twice sub-boiled concentrated HNO_3.

2.32. Background information on the growth of siboglinid tubeworms and associated redox processes

Siboglinid tubeworms include some of the longest-lived animals on earth, with life spans extending up to 300 yr old (*e.g.*, Bergquist et al., 2000; Durkin et al., 2017). While the mode of growth of siboglinid tubeworms still remains poorly constrained, it is generally assumed that the tube can grow at both ends (*e.g.*, Gaill et al., 1997), resulting in the formation of successive concentric growth lines in the anterior extension of the tube that is bathed by ambient bottom waters. In situ growth measurements suggest that the tube of siboglinid annelids grows at an average rate of ~1 cm/yr (*e.g.* Bergquist et al., 2000; Cordes et al., 2005; Cordes et al., 2007; Durkin et al., 2017). The chitin-producing glands are located in the anterior end of the animal, associated with a muscular organ called the vestimentum (*e.g.*, Bright and Lallier, 2010). Several studies have suggested that chitin and protein dissolution may occur in the basal part of the animal due to secretion of enzymes (*e.g.*, Gaill et al., 1997).

At cold seeps, all species of siboglinid worms share a common habitat, living at the redox interface between oxic bottom waters and the reduced sediment. As mentioned above, a

126 preliminary set of data (Fe, Mn, Zr, Sr) has been already reported for the same tube of
127 *Escarpia southwardae* investigated in this study (Duperron et al., 2014), indicating the
128 presence of two distinct oxidation fronts along the tube. As inferred from Mn and Fe
129 concentrations (Fig. 2), a first redox front was shown to occur near the posterior root-like
130 extension of the tube (between sections S45-S49), corresponding to the redox interface
131 between oxic bottom waters and the anoxic sediment. In marine sediments, early diagenetic
132 processes proceed with the reduction of hydrogenous Fe-Mn oxyhydroxide phases under
133 oxygen-depleted conditions (*e.g.*, Burdige, 1993). In organic-rich sediments or in areas
134 influenced by methane seepage, this process typically occurs within the first tens of
135 centimetres below the seafloor, releasing dissolved Mn^{2+} and Fe^{2+} into the surrounding pore
136 waters, which then diffuse upwards until they re-precipitate as diagenetic Fe-Mn
137 oxyhydroxides, when oxic conditions are met again near the seafloor or in bottom waters
138 (*e.g.*, Burdige, 1993; Schulz et al., 1994; Bayon et al., 2011a; Pop-Ristova et al., 2012). A
139 second oxidative front was also identified at the anterior end of the tube (S1-S8), inferred
140 solely from Mn concentrations (Fig. 2), interpreted as the result of active oxygen uptake by
141 the branchial plume (Duperron et al., 2014). As proposed in this latter study, intense oxygen
142 consumption in the branchial plume region most likely result in a micro-redox gradient that
143 could locally foster microbial activity, possibly playing a key role in the metabolism of
144 siboniglids.

145

146 *2.3. Methods*

147 Concentrations for rare earth and other trace elements were determined at the Pôle
148 Spectrométrie Océan (Brest, France) on an Element2 ICP-MS, after addition of a Tm spike
149 and correction for polyatomic oxide and hydroxide interferences (Barrat et al., 1996). The
150 precision and accuracy of our measurements were assessed by replicate analyses of the MA-

A-1/TM certified reference material (International Atomic Energy Agency; IAEA). MA-A-1 corresponds to homogenized copepods (*Calanus cristatus*) collected from the Norwegian Sea and composed of chitin. Precision (expressed as relative standard deviation in Table 1) was better than 15% RSD for most elements, except Zr (18.7%), Mo (24%), Gd (18.1%) and Th (15.8%). The accuracy of our procedure was evaluated by comparing our results to recommended values for V, Mn, Fe, Co, Ni, Cu and Zn (Table 1; International Atomic Energy Agency, 1990; Maher et al., 2001), demonstrating relatively good agreement (within 15%) except for V (24%). For other elements, the accuracy was assessed by analysing MA-A-1 after an additional step of iron oxide co-precipitation; a method that allows quantitative extraction of reactive trace elements (including REE) and separation from the sample matrix, resulting in accurate results for various geological samples (Bayon et al., 2009a; Bayon et al., 2011b). The good agreement obtained between the two datasets (Table 1) further validates our procedure for the following elements: Mn, Y, REE and Th. The REE concentrations were normalized to World River Average Silt (WRAS) abundances (Bayon et al., 2015). The La and Ce enrichments in studied sections of the tube were quantified using the shale-normalized ($_N$) La (La/La*) and (Ce/Ce*) anomalies, where La* and Ce* correspond to theoretical concentrations calculated geometrically assuming that the behaviour of their respective REE neighbours is linear on a log-linear plot (Lawrence et al., 2006), with $La^* = Pr_N \times (Pr_N/Nd_N)^2$ and $Ce^* = Pr_N \times (Pr_N/Nd_N)$, respectively. Positive and negative La and Ce anomalies are indicated by La/La* and Ce/Ce* > 1 and < 1, respectively.

3. Results

Measured trace element abundances in the tube sections are reported in Table 2. Selected elemental profiles for REE (La, Gd) and other trace elements (Mn, Fe, Th, V, Mo, U and Cu) along the tube are presented in Fig. 2. As previously shown for Fe and Zr (Duperron et al.,

176 2014), Th and other elements typically associated with the silicate detrital fraction of the
177 sediment (*e.g.*, Rb, Ba) display marked enrichments in both anterior and posterior extensions
178 of the tube (Fig. 2). The REE also display similar concentration profiles (*e.g.*, La, Gd; Fig. 2),
179 with La abundances fluctuating over more than one order of magnitude between the anterior
180 end of the tube (319 ng/g in section S1), to its middle (21 ng/g; S30) and posterior (417 ng/g;
181 S55) parts. However, while high Gd abundances in the anterior portion of the tube mainly
182 occur in sections S1 and S2, the observed La enrichment extends down to section S22
183 approximately, as clearly shown by higher $(La/Gd)_N$ in this portion of the tube (Fig. 2). Note
184 that the La and Gd (and other REE) also exhibit a small enrichment at ~ 85 cm, similar to that
185 previously observed for Mn and Fe (Duperron et al., 2014). Copper exhibits a slightly
186 different profile along the tube, characterized by high concentrations in the anterior part (> 10
187 µg/g in sections S1-2) and a smooth decrease in the remaining part of the tube. Finally, the
188 three redox sensitive elements (V, Mo and U) display markedly different elemental profiles
189 along the tube, with their lowest concentrations being observed in the anterior extension of the
190 tube (Fig. 2). Along the tube, V, Mo and U display similar trends until ~80 cm, characterized
191 by a sudden increase of concentrations in the anterior part of the tube (*e.g.*, from ~ 0.2 to 10
192 µg/g for U), followed by a gentle decrease to reach minimum values between sections S22
193 and S44. Below the seawater-sediment interface (~80 cm), Mo and V abundances increase
194 steadily, while U concentrations remain near constant (Fig. 2).

195

196 **4. Discussion**

197 *4.1. U, Mo and V constraints on changing redox conditions along the tube*

198 Our new set of data includes trace elements (V, Mo and U) that are more soluble in oxic
199 environments than under oxygen-depleted conditions (for a detailed review of the behaviour
200 of redox-sensitive elements in the marine environment, see Tribovillard et al., 2006 and

Smrzka et al., 2019). These redox elements are typically enriched in reduced organic-rich sediments, being relatively unaffected by the presence of detrital silicate minerals. As such, they are commonly used in sedimentary records as paleoproductivity and/or paleoredox proxies (*e.g.*, Algeo and Maynard, 2004; Tribovillard et al., 2006). In seepage areas, the presence of significant Mo and U enrichments in sub-surface sediment horizons has been also interpreted as reflecting fossil evidence for past circulation events of methane-rich fluids (Peketi et al., 2012; Sato et al., 2012; Hu et al., 2015; Chen et al., 2016). In the marine environment, both Mo and V share strong affinities with Mn oxides and, as a consequence, are strongly affected by the redox cycling of Mn at the seawater-sediment interface (*e.g.*, Calvert and Pedersen, 1993; Crusius et al., 1996). Under oxygen-depleted conditions, increasing levels of dissolved sulphide typically lead to enhanced sequestration of Mo and V into various organic compounds and sulphide minerals in the sediment (*e.g.*, Tribovillard et al., 2006). Unlike Mo and V, the enrichment of U in reduced marine sediments is not influenced by the redox cycling of Fe-Mn oxyhydroxides, nor does it reflect the levels of dissolved hydrogen sulphide in the surrounding environment (*e.g.*, Algeo and Maynard, 2004; McManus et al., 2005).

Based on the above, the steady increase of V, Mo and U concentrations starting from the most anterior part of the tube (i.e. the 'upper' 10 cm, between S1 and S8) is best explained as reflecting a sharp redox gradient between oxic bottom waters (where V, Mo and U are mostly present in soluble forms) and the branchial plume region associated with intense oxygen consumption (where oxygen-depleted conditions are expected to result in the preferential immobilization of these redox-sensitive elements). Due to their known affinity with Mn, it is also possible that some of the observed enrichments for V and Mo in this part of the tube also partly relate to the redox cycling of Mn. Between ~10 and 80 cm, the progressively

decreasing V and Mo concentrations along the tube (and to a lesser extent U) presumably reflect the presence of less reduced conditions, although the persistence of relatively high U concentrations in this portion of the tube may still point towards relatively low oxygen levels. Finally, in the posterior part of the tube rooted in the sediment, below ~80 cm, the sharp increase of Mo concentrations (and to a lesser extent V) most likely indicates the presence of high levels of dissolved sulphide below the seawater-sediment interface. Overall, the interpretations based on the use of these three redox-sensitive elements agree well with the hypothesis proposed earlier by Duperron et al. (2014), confirming that siboglinid tubes are associated with the presence of sharp redox gradients at both posterior and anterior extensions.

4.2. Pore water versus seawater REE signatures along the siboglinid tube

In sections S1 and S2, high La and other REE abundances are best explained by the presence of detrital particles embedded within the chitin-rich matrix, as inferred both from corresponding high contents of Th and other terrigenous elements (Fig. 2; Table 2) and relatively flat shale-normalized REE distribution patterns (Fig. 3a). This recently-secreted portion of the tube is indeed much thinner than the rest of the chitinous tube (except for its posterior root-like extension; Duperron et al., 2014), and hence most likely to be 'contaminated' with particles derived from ambient turbid bottom waters. Below the seawater-sediment interface (between S45-S55), the observed increasing REE abundances could also reflect to some extent the presence of detrital particles, but also, presumably, the acquisition by the chitin tube of dissolved REE from surrounding pore waters. At ocean margins, anoxic pore waters typically display mid-REE (MREE) enrichments and positive Ce anomalies as a result of the reductive dissolution of Fe-Mn oxyhydroxide phases (*e.g.*, Sholkovitz et al., 1989; Haley et al., 2004; Himmler et al., 2013; Abbott et al., 2015), with

corresponding distribution patterns that closely resemble those determined in the most posterior sections of *Escarpia southwardae* (Fig. 3d). Instead, the anterior part of the tube, located above the seawater-sediment interface, is characterized by REE distribution patterns exhibiting a progressive increase of heavy-REE relative to the LREE; a feature that is typical of seawater (Fig. 3d). This feature is most apparent in the portion of the tube located between sections S22-S44 (Fig. 3c), where REE exhibit shale-normalized signatures very similar to that of ambient seawater, including the presence of pronounced negative Ce anomalies (Lemaitre et al., 2014; see the red dotted line in Fig. 3d). Taken together, these characteristics indicate that ambient bottom waters most likely acted as the main source of dissolved REE in this portion of the tube.

The relative influence of pore water *versus* seawater REE signatures in the studied siboglinid tube can be further constrained using both Ce and La anomalies. Along the tube, Ce anomalies display a general trend from positive (> 1) to negative (< 1) Ce/Ce* values from its apical end to ~ 75 cm, followed, below the seawater-sediment interface, by a marked increase up to Ce/Ce* ~ 1.4 (Fig. 2). Except for the first two sections S1-S2, La anomalies display a similar depth-profile in the anterior part of the tube, characterized by a gradual decrease from high (~ 3-4) to low (~ 1-2) La/La* values (Fig. 2). However, in contrast to Ce/Ce*, La anomalies remain at low La/La* values (~ 1-2) below the seawater-sediment interface, except for two samples (S51 and S52). This decoupling between Ce and La anomalies can be also illustrated in a Ce/Ce* vs La/La* graph (Fig. 4), where our results for the tube sections are compared to an extensive compilation of literature data for pore waters and seawater (see Tables S1 and S2). Apart from sections S51 and S52, all the sections derived from the buried posterior extension of the tube clearly plot within the field defined by pore waters, while sections from the tube interval between sections S22 and S44 plot within the field of seawater.

This latter observation agrees well with the hypothesis that seawater actively circulates within the tube (Cordes et al, 2005; Duperron et al, 2014). In Fig. 4, the tube sections between S22 and S44 are aligned along a general mixing relationship defined by bottom waters at Regab, from both the seafloor (<1m elevation) and the overlying water column (>1m), and pore waters, which suggests that while ambient waters probably act as a major source of REE in the anterior part of the tube, their REE signature is also probably partially influenced by pore waters.

4.3. Evidence for microbial utilization of LREE related to aerobic oxidation of methane

A striking feature of Fig. 4 is that most sections from the most anterior part of the tube depart significantly from the 'seawater & pore water' array, displaying higher-than-normal La anomalies. Between S3 and S21, changing REE abundances are also reflected by flatter shale-normalized patterns and the absence of negative Ce anomalies (Fig. 3a,b), indicating that REE decoupling probably occurs along this section of the tube. It is unlikely that this change in shale-normalized patterns results from co-precipitation onto Mn oxyhydroxide phases, as could be possibly inferred from increasing Mn contents in the same part of the tube. If this was the case, one would expect similarly corresponding enrichments in trace elements such as Co, which generally share strong affinities for Mn oxides (Table 2). Additionally, any authigenic Mn-oxide phase associated with the chitin tube would be expected to display a shale-normalized REE pattern similar to that of anoxic pore waters, hence without any particular La anomalies. This is illustrated by the fact that leached Fe-Mn oxyhydroxide phases from surficial Congo Fan sediments (Bayon et al., 2004) plot well within the field of pore waters in Fig. 4. Instead, we propose below that the light-REE enrichments observed in the anterior portion of the tube could be related to microbial processes.

There is plentiful evidence that active microbial activity takes place in the anterior part of siboglinid tubes at cold seeps. For instance, recent studies conducted at methane seeps recently identified Methylococcales and other methanotrophic bacteria as an abundant microbial group in the anterior portion of chitin tubes of siboglinids, including *Escarpia southwardae* (Medina-Silva et al., 2018; Rincón-Tomás et al., 2020). In addition to the primary sulphur-oxidizing symbionts present in the animal itself, the presence of abundant methanotrophic bacteria in the upper part of the tube of a *Lamellibrachia* species was also supported using methanotroph-specific molecular probes and sequencing of a subunit of methane monooxygenase (Duperron et al., 2009). While the nutritional role of these tube-associated bacteria to their siboglinid hosts remains largely unknown (Hilario et al., 2011), all the above evidence collectively suggest that methanotrophs are common colonizers of the tubes of seep tubeworms worldwide, which could possibly contribute to the biomineralization of the tube (. Like other families of aerobic methane-oxidising bacteria, most Methylococcales possess both the methane monooxygenase (MMO) and methanol dehydrogenase (MDH) enzymes, which catalyse the oxidation of methane to methanol and subsequent conversion to formaldehyde, respectively (*e.g.*, Semrau et al., 2018). As mentioned in the Introduction, the activity of the XoxF-type of methanol dehydrogenase is now known to be strongly dependent on light-REE availability, especially La and Ce. Instead, the first step of methane oxidation is mostly controlled by copper availability. When Cu is abundant, methanotrophs express a membrane-bound Cu-containing enzyme called particulate methane monooxygenase (pMMO), which catalyzes the oxidation of methane to methanol (*e.g.*, Glass and Orphan, 2012). In the studied tube of *Escarpia southwardae*, the abundance profile for Cu closely follows that for La (Fig. 2). Additionally, Cu contents, after normalization to Th in order to correct from any effect related to the presence of detrital particles, also display strong positive relationships with both La/Th and shale-normalized La

anomaly (Fig. 5). To a lesser extent, Cu also shows positive correlations with Ce/Th ratios and Ce/Ce* in the anterior region of the studied tube, hence suggesting that these two elements are also involved in the same biogeochemical processes along the tube. While the magnitude of measured Ce anomalies along the studied tube is likely to be strongly influenced by various diagenetic processes (presence of Mn oxyhydroxide phases) and source effects (relative seawater *versus* pore water contributions), this observation is consistent with previous investigations, which suggested that both La and Ce can be transported and used at similar rates by methanotrophs and methylotrophs (e.g. Pol et al., 2014; Semrau, 2018; Daumann, 2019; Picone and Op den Camp, 2019). Therefore, in agreement with our recent findings on chemosynthetic mussels from the South China Sea (Wang et al., 2020), the above lines of evidence strongly suggest that the aerobic oxidation of methane at cold seeps can result in the combined uptake of both dissolved light-REE and Cu in the anterior extension of cold seep siboglinid tubes.

4.4. Revisiting REE systematics in modern cold seep carbonates

Unlike the Gulf of Mexico, where intense LREE scavenging had occurred in the water column following the *Deepwater Horizon* oil spill, no significant LREE depletion was identified in the bottom waters at Regab (Lemaitre et al., 2014). The massive amounts of methane accidentally released during the *Deepwater Horizon* disaster (Joye et al., 2011) possibly accounted for as much as a few percent of the total flux of natural CH_4 emitted from the seafloor at ocean margins annually (Boetius and Wenzhöfer, 2013), resulting locally in unprecedented high rates of methane oxidation into the water column (Crespo-Medina et al., 2014). Instead, at natural submarine seeps, *anaerobic* oxidation of methane represents an effective filter for CH_4 in the sediment (Boetius and Wenzhöfer, 2013), so that rates of *aerobic* methane oxidation in the overlying water column are consequently much reduced. At

Regab, the absence of any dissolved REE enrichment in bottom waters contrasted with the behaviour of Mn and Fe, which both displayed significantly higher dissolved contents in the water column overlying seepage sites (Lemaitre et al., 2014). This discrepancy between elements generally exhibiting relatively similar geochemical behaviour in the marine environment was interpreted as reflecting preferential removal of REE during precipitation of authigenic carbonates in sub-surface sediments (Lemaitre et al., 2014). In the light of our findings, future investigations should also investigate whether microbial REE uptake by chemosynthtic communities could also account, at least to some extent, for REE removal at cold seeps.

To further evaluate the hypothesis that aerobic methane oxidation can drive preferential utilization of LREE at submarine methane seeps, we also re-examine the available set of REE data for modern cold seep carbonates worldwide, which complements the recent literature review by Smrzka et al. (2020). At cold seeps, authigenic carbonates represent a direct by-product of the anaerobic pathway for methane oxidation (AOM), resulting from enhanced alkalinity and carbonate saturation levels in the surrounding pore waters (*e.g.*, Aloisi et al., 2002). The type and mineralogical composition of authigenic carbonates is strongly dependent upon the upward methane flux and the depth at which the AOM takes place within the sediment; the so-called sulphate-methane transition zone (SMTZ). In areas of high CH_4 fluxes, AOM typically proceeds near the seafloor, resulting in the formation of massive carbonate pavements dominated by aragonite and associated with abundant chemosynthetic fauna (*e.g.*, Greinert et al., 2001; Naehr et al., 2007). In contrast, in areas of reduced methane seepage, the depth of the SMTZ is encountered deeper within the sediment column (e.g., Borowski et al., 1996), where AOM and the presence of sulphate-depleted conditions are typically accompanied by the formation of homogeneous nodules of high-Mg carbonates,

such as high-Mg calcite, dolomite or siderite (*e.g.*, Aloisi et al., 2002; Gieskes et al., 2005; Bayon et al., 2007; Naehr et al., 2007). Despite of the genetic link between AOM and authigenic carbonates at cold seeps, the formation of aragonite at the seafloor has been occasionally associated with the presence of oxic conditions, at least locally, as inferred from the occurrence of negative Ce anomalies and various molecular fossils (biomarkers) of aerobic methanotrophic bacteria (*e.g.*, Birgel et al., 2011; Himmler et al., 2015). As such, seafloor carbonate pavements can represent potential archives for searching additional evidence of the preferential microbial utilization of LREE through aerobic methane oxidation.

In Fig. 6, we investigate the relationships between Ce/Ce* and La/La* in modern cold seep carbonates worldwide (Feng et al., 2008, 2009a, 2010; Himmler et al., 2010; Birgel et al., 2011; Rongemaille et al., 2011; Bayon et al., 2013; Hu et al., 2014; Pierre et al., 2014; Wang et al., 2014, 2015; Novikova et al., 2015; Crémière et al., 2016 ; Franchi et al., 2017 ; Yang et al., 2018; Smrzka et al., 2019 ; Wang et al., 2019). Note that all these literature data for modern seep carbonates are also compiled in Table S3. Authigenic carbonates were classified into two groups depending on their dominant mineralogy: aragonite and high-Mg carbonates. As expected, high-Mg carbonates clearly plot within the field of pore waters in Fig. 6a, yielding average La and Ce anomalies of 1.14 ± 0.30 and 1.09 ± 0.24 (1SD; n=160), respectively. Most aragonite crusts at cold seeps also plot in the field of pore waters, but exhibit slightly lower Ce anomalies (0.97 ± 0.31) and higher La/La* average values (1.21 ± 0.31; n=114). In Fig. 6a, a few aragonite samples associated with low Ce anomalies, hence displaying a seawater-like REE signature, also appear to exhibit slightly higher La anomalies (with La/La* > ~1.5). However, these values remain within the observed range of La/La* values in seawater (between ~ 1 and 3), so their interpretation in terms of preferential La microbial utilization cannot be conclusive.

In Fig. 6b, we also examine the relationships between shale-normalized La/Gd and Gd/Yb ratios in the same set of seep carbonate samples. As recently shown (Bayon et al., 2020), this graph is particularly well suited for investigating the general shape of shale-normalized REE patterns, especially for discriminating between samples exhibiting a typical MREE bulge of anoxic pore waters (characterized by relatively low $(La/Gd)_N$ and high $(Gd/Yb)_N$ values) and those displaying seawater-like patterns (characterized by both low $(La/Gd)_N$ and high $(Gd/Yb)_N$ values). In Fig. 6b, the observed range of $(La/Gd)_N$ and $(Gd/Yb)_N$ values in high-Mg carbonates also remarkably overlaps with pore water data. However, while most aragonite concretions do display similar $(La/Gd)_N$ and $(Gd/Yb)_N$ values, many of them appear to depart significantly from the fields defined by pore waters and seawater, being characterized by substantially higher shale-normalized La/Gd ratios (up to ~ 2.2; Fig. 6b). A similar observation can be drawn when plotting $(Pr/Gd)_N$ versus $(Gd/Yb)_N$ for the same set of authigenic carbonate samples (graph not shown here), indicating that these particular samples are also enriched in other LREE relative to the MREE.

A shared characteristic of those carbonate samples with high $(La/Gd)_N$ ratios is that they correspond to aragonite-rich seafloor carbonate pavements from the Gulf of Mexico (Feng et al., 2009a; Birgel et al., 2011; Hu et al., 2014; Smrzka et al., 2019), the Niger delta (Rongemaille et al., 2011; Wang et al., 2019), the Makran accretionary prism (Himmler et al., 2010), and the Mediterranean Sea (Franchi et al., 2017), which are all closely associated with abundant chemosynthetic fauna (*e.g.*, bathymodiolin mussels, tube worms) that live in symbiosis with aerobic methane-consuming microbes (*e.g.*, Aharon, 1994; Greinert et al., 2001; Teichert et al., 2005; Han et al., 2008). On this basis, the occurrence of anomalously high $(La/Gd)_N$ in chemoherm carbonates at cold seeps could possibly reflect the presence of shell fragments bearing the REE signature of the aerobic oxidation of methane. However, considering the recent REE data obtained on methanotrophic mussels from the South China

Sea (with a mean shale-normalized La/Gd ratio ~ 3.7; Wang et al., 2020), this hypothesis would be quite unlikely because REE concentrations in the carbonate shells are depleted by about two orders of magnitude compared to seep carbonates. In the Gulf of Mexico, the occurrence of pronounced LREE enrichments has been documented in laser-ablated aragonite phases from carbonate pavements associated with asphalt volcanism, interpreted as reflecting the degradation of liquid hydrocarbons (Smrzka et al., 2019; Fig. 6b). As proposed in that latter study, such LREE enrichments could be taken as diagnostic features for the influence of oil seepage at seep sites. Additionally, the presence of LREE enrichments in seafloor aragonite concretions could also reflect their close association with the chemosynthetic biomass, as proposed recently in an investigation of ancient seep carbonates by laser-ablation ICP-MS (Zwicker et al., 2018; Fig. 6b). At cold seeps, spectacular LREE enrichments have been indeed identified in the soft tissues of chemosynthetic mussels (with shale-normalized La/Gd ratios of up to ~ 100), which were clearly attributed to reflecting the signature of REE-dependent methanotrophy (Wang et al., 2020). Seafloor carbonate pavements are typically traversed by a dense network of tubular holes, which marks the presence of ancient siboglinid tubeworms whose tubes have now been dissolved (*e.g.*, Feng and Roberts, 2010; Feng et al., 2013). This process probably occurs over short timescales (a few decades or centuries) because recent carbonate crusts (as inferred from U-Th dating) commonly display the same petrographic features (*e.g.*, Bayon et al., 2009b). Based on the above, we suggest that the degradation of chitin tubes and/or other organic compounds bearing the geochemical signature of lanthanide-dependent methanotrophy could possibly result locally in the release of LREE-enriched dissolved signatures that would be subsequently incorporated into authigenic aragonite. Such a process could possibly account for some of the observed LREE enrichments in modern seep carbonates, in addition to providing a plausible explanation for

450 the presence of ‘aerobic’ geochemical signatures in authigenic carbonates formed otherwise
451 via AOM.

452

453 **5. Concluding remarks and future perspectives**

454 Our high-resolution trace element investigation of a one-meter long chitin tube of a deep-
455 sea siboglinid worm provides new evidence for the occurrence of aerobic microbial utilization
456 of light-REE at cold seeps. In the branchial plume region of the tubeworm, the combined
457 uptake of both Cu and LREE (especially La and Ce) from ambient seawater is inferred to be
458 associated with the presence of tube-associated methane-consuming bacteria, serving as
459 metalloenzymes for the transformation of methane to methanol, and subsequent conversion to
460 formaldehyde, respectively. A reassessment of REE data for modern authigenic carbonates
461 worldwide also suggests discernible signatures of lanthanide-dependent methanotrophy in
462 many seafloor aragonite pavements, as inferred from the presence of anomalously high La
463 contents compared to other REE (with shale-normalized La/Gd ratios > ~ 0.8). Such LREE
464 enrichments in seep carbonates could possibly reflect the acquisition of geochemical
465 signatures inherited from the degradation of chemosynthetic biomass supported by REE-
466 dependent methanotrophy.

467 In future studies, we anticipate that these findings and their application to fossil microbial
468 carbonates could provide new insights into the biogeochemical processes operating in ancient
469 oceans. This could include the re-evaluation of previous REE datasets for ancient seep
470 carbonates (*e.g.*, Feng et al., 2009b; Tong and Chen, 2012; Tribovillard et al., 2013; Della
471 Porta et al., 2015; Colin et al., 2015; Smrzka et al., 2016; Zwicker et al., 2018; Argentino et
472 al., 2019; Zhu et al., 2019), but also for various microbial archives of Precambrian oceans, at
473 times when methane levels were presumably much higher both in the atmosphere and oceans
474 (*e.g.*, Catling et al., 2001; Konhauser et al., 2009). For instance, many Late Archaean

475 stromatolites also display marked enrichments in La and other LREE (e.g., Kamber and
476 Webb, 2001; Planavsky et al., 2010; Kamber et al., 2014; Schier et al., 2018). Future work
477 could aim at investigating whether these particular features, generally taken as evidence for
478 the presence of severely depleted oxygen levels in shallow waters (*e.g.*, Kamber et al., 2014),
479 could also possibly correspond to the geochemical imprint of lanthanide-dependent
480 methanotrophy in early Earth's oceans.

481

482 **Acknowledgments**

483 We thank the crews of R/V *Pourquoi Pas?* and all participants of the WACS cruise (2011; PI:
484 Karine Olu-Leroy) for their assistance at sea. Claire Bassoulet is warmly acknowledged for
485 assistance during ICPMS measurements. We also thank the Editor (Michael Boettcher),
486 Tobias Himmler and two anonymous reviewers for providing insightful comments on this
487 manuscript. This work was funded by IFREMER.

488

489 **References**

490 Abbott, A.N., Haley, B.A., McManus, J., Reimers, C.E., 2015. The sedimentary flux of
491 dissolved rare earth elements to the ocean. Geochim. Cosmochim. Acta 154, 186-200.
492 Aharon, P., 1994. Geology and biology of modern and ancient submarine hydrocarbon seeps
493 and vents: an introduction. Geo-Mar. Lett. 14, 69-73.
494 Algeo, T.J., Maynard, J.B., 2004. Trace-element behavior and redox facies in core shales of
495 Upper Pennsylvanian Kansas-type cyclothems. Chem. Geol. 206, 289-318.
496 Aloisi, G., Bouloubassi, I., Heijs, S.K., Pancost, R.D., Pierre, C., Damsté, J.S.S., Gottschal,
497 J.C., Forney, L.J., Rouchy, J. M., 2002. CH_4-consuming microorganisms and the formation
498 of carbonate crusts at cold seeps. Earth Planet. Sci. Lett. 203, 195-203.

499 Andersen, A.C., Hourdez, S., Marie, B., Jollivet, D., Lallier, F.H., Sibuet, M., 2004. Escarpia
500 southwardae sp. nov., a new species of vestimentiferan tubeworm (Annelida, Siboglinidae)
501 from West African cold seeps. Canad. J. Zool. 82, 980-999.
502 Argentino, C., Lugli, F., Cipriani, A., Conti, S., Fontana, D., 2019. A deep fluid source of
503 radiogenic Sr and highly dynamic seepage conditions recorded in Miocene seep carbonates
504 of the northern Apennines (Italy). Chem. Geol. 522, 135-147.
505 Barrat, J.A., Keller, F., Amosse, J., Taylor, R.N., Nesbitt, R.W., Hirata, T., 1996.
506 Determination of rare earth elements in sixteen silicate reference samples by ICP-MS after
507 Tm addition and ion exchange separation. Geostand. Newslett. 20, 133-139.
508 Bayon, G., German, C.R., Burton, K.W., Nesbitt, R.W., Rogers, N., 2004. Sedimentary Fe–
509 Mn oxyhydroxides as paleoceanographic archives and the role of aeolian flux in
510 regulating oceanic dissolved REE. Earth Planet. Sci. Lett. 224, 477-492.
511 Bayon, G., Pierre, C., Etoubleau, J., Voisset, M., Cauquil, E., Marsset, T., Sultan, N., Le
512 Drezen, E., Fouquet, Y., 2007. Sr/Ca and Mg/Ca ratios in Niger Delta sediments:
513 implications for authigenic carbonate genesis in cold seep environments. Mar. Geol. 241,
514 93-109.
515 Bayon, G., Barrat, J.A., Etoubleau, J., Benoit, M., Bollinger, C., Révillon, S., 2009a.
516 Determination of rare earth elements, Sc, Y, Zr, Ba, Hf and Th in geological samples by
517 ICP-MS after Tm addition and alkaline fusion. Geostand. Geoanal. Res. 33, 51-62.
518 Bayon, G., Henderson, G.M., Bohn, M., 2009. U–Th stratigraphy of a cold seep carbonate
519 crust. Chem. Geol. 260, 47-56.
520 Bayon, G., Birot, D., Ruffine, L., Caprais, J.C., Ponzevera, E., Bollinger, C., Donval, J.P.,
521 Charlou, J.L., Voisset, M., Grimaud, S., 2011a. Evidence for intense REE scavenging at
522 cold seeps from the Niger Delta margin. Earth Planet. Sci. Lett. 312, 443-452.

523 Bayon, G., Birot, D., Bollinger, C., Barrat, J.A., 2011b. Multi-element determination of trace
524 elements in natural water reference materials by ICP-SFMS after Tm addition and iron co-
525 precipitation. Geostand. Geoanal. Res. 35, 145-153.
526 Bayon, G., Dupré, S., Ponzevera, E., Etoubleau, J., Chéron, S., Pierre, C., Mascle, J., Boetius,
527 A., De Lange, G.J., 2013. Formation of carbonate chimneys in the Mediterranean Sea
528 linked to deep-water oxygen depletion. Nat. Geosci. 6, 755-760.
529 Bayon, G. et al., 2015. Rare earth elements and neodymium isotopes in world river sediments
530 revisited. Geochim. Cosmochim. Acta 170, 17-38.
531 Bayon, G., Lambert, T., Vigier, N., De Deckker, P., Freslon, N., Jang, K., Larkin, C.S.,
532 Piotrowski, A.M., Tachikawa, K., Thollon, M., Tipper, E.T., 2020. Rare earth element and
533 neodymium isotope tracing of sedimentary rock weathering. Chem. Geol. 553, 119794.
534 Bergquist, D.C., Williams, F.M., Fisher, C.R., 2000. Longevity record for deep-sea
535 invertebrate. Nature 403, 499-500.
536 Birgel, D., Feng, D., Roberts, H.H., Peckmann, J., 2011. Changing redox conditions at cold
537 seeps as revealed by authigenic carbonates from Alaminos Canyon, northern Gulf of
538 Mexico. Chem. Geol. 285, 82-96.
539 Boetius, A., 2005. Microfauna-macrofauna interaction in the seafloor: lessons from the
540 tubeworm. PLoS Biol. 3, e102.
541 Boetius, A., Wenzhöfer, F., 2013. Seafloor oxygen consumption fuelled by methane from
542 cold seeps. Nat. Geosci. 6, 725-734.
543 Borowski, W.S., Paull, C.K., Ussler III, W., 1996. Marine pore-water sulfate profiles indicate
544 in situ methane flux from underlying gas hydrate. Geology 24, 655-658.
545 Bowen, H.J.M., 1966. Trace Elements in Biochemistry. Academic Press, London and
546 New York.

547 Bright, M., Lallier, F.H., 2010. The biology of vestimentiferan tubeworms. Oceanogr. Mar.
548 Biol. 48, 213-266.
549 Burdige, D. J., 1993. The biogeochemistry of manganese and iron reduction in marine
550 sediments. Earth Sci. Rev. 35, 249-284.
551 Calvert, S.E., Pedersen, T.F., 1993. Geochemistry of recent oxic and anoxic marine
552 sediments: implications for the geological record. Mar. Geol. 113, 67-88.
553 Catling, D.C., Zahnle, K.J., McKay, C.P., 2001. Biogenic Methane, Hydrogen Escape, and the
554 Irreversible Oxidation of Early Earth. Science 293, 839-843.
555 Charlou, J. L. et al., 2004. Physical and chemical characterization of gas hydrates and
556 associated methane plumes in the Congo–Angola Basin. Chem. Geol. 205, 405-425.
557 Chen, F., Hu, Y., Feng, D., Zhang, X., Cheng, S., Cao, J., Lu, H., Chen D., 2016. Evidence of
558 intense methane seepages from molybdenum enrichments in gas hydrate-bearing sediments
559 of the northern South China Sea. Chem. Geol. 443, 173–181.
560 Collin, P.Y., Kershaw, S., Tribovillard, N., Forel, M.B., Crasquin, S., 2015. Geochemistry of
561 post-extinction microbialites as a powerful tool to assess the oxygenation of shallow
562 marine water in the immediate aftermath of the end-Permian mass extinction. Int. J. Earth
563 Sci. 104, 1025-1037.
564 Cordes E.E., Arthur M.A., Shea K., Fisher C.R., 2005. Modeling the mutualistic interactions
565 between tubeworms and microbial consortia. PLoS Biol. 3, 497–506.
566 Cordes, E.E., Bergquist, D.C., Redding, M.L., Fisher, C.R., 2007. Patterns of growth in cold-
567 seep vestimenferans including Seepiophila jonesi: a second species of long-lived
568 tubeworm. Mar. Ecol. 28, 160-168.
569 Crémière, A. et al., 2016. Fluid source and methane-related diagenetic processes recorded in
570 cold seep carbonates from the Alvheim channel, central North Sea. Chem. Geol. 432, 16-
571 33.

572 Crespo-Medina, M. et al., 2014. The rise and fall of methanotrophy following a deepwater oil-
573 well blowout. Nat. Geosci. 7, 423-427.
574 Crusius, J., Calvert, S., Pedersen, T., Sage, D., 1996. Rhenium and molybdenum enrichments
575 in sediments as indicators of oxic, suboxic and sulfidic conditions of deposition. Earth
576 Planet. Sci. Lett. 145, 65-78.
577 Della Porta, G., Webb, G.E., McDonald, I., 2015. REE patterns of microbial carbonate and
578 cements from Sinemurian (Lower Jurassic) siliceous sponge mounds (Djebel Bou Dahar,
579 High Atlas, Morocco). Chem. Geol. 400, 65-86.
580 Duperron, S. , De Beer, D., Zbinden, M., Boetius, A., Schipani, V., Kahil, N., Gaill, F., 2009.
581 Molecular characterization of bacteria associated with the trophosome and the tube of
582 *Lamellibrachia* sp., a siboglinid annelid from cold seeps in the eastern Mediterranean.
583 FEMS Microbiol. Ecol. 69, 395-409.
584 Duperron, S., Gaudron, S.M., Lemaitre, N., Bayon, G., 2014. A microbiological and
585 biogeochemical investigation of the cold seep tubeworm *Escarpia southwardae* (Annelida:
586 Siboglinidae): Symbiosis and trace element composition of the tube. Deep Sea Res. Part I
587 Oceanogr. 90, 105-114.
588 Durkin, A., Fisher, C.R., Cordes, E.E., 2017. Extreme longevity in a deep-sea vestimentiferan
589 tubeworm and its implications for the evolution of life history strategies. Sci. Nat-
590 Heidelberg 104, 63.
591 Feng, D., Roberts, H.H., 2010. Initial results of comparing cold-seep carbonates from mussel-
592 and tubeworm-associated environments at Atwater Valley lease block 340, northern Gulf
593 of Mexico. Deep-Sea Res. Part II-Top. Stud. Oceanogr. 57, 2030-2039.
594 Feng, D., Chen, D., Qi, L., Roberts, H.H., 2008. Petrographic and geochemical
595 characterization of seep carbonate from Alaminos Canyon, Gulf of Mexico. Chin. Sci.
596 Bull. 53, 1716-1724.

Feng, D., Chen, D., Roberts, H.H., 2009a. Petrographic and geochemical characterization of seep carbonate from Bush Hill (GC 185) gas vent and hydrate site of the Gulf of Mexico. Mar. Petrol. Geol. 26, 1190-1198.

Feng, D., Chen, D., Peckmann, J., 2009b. Rare earth elements in seep carbonates as tracers of variable redox conditions at ancient hydrocarbon seeps. Terr. Nova 21, 49-56.

Feng, D., Chen, D., Peckmann, J., Bohrmann, G., 2010. Authigenic carbonates from methane seeps of the northern Congo fan: microbial formation mechanism. Mar. Petrol. Geol. 27, 748-756.

Feng, D., Cordes, E.E., Roberts, H.H., Fisher, C.R., 2013. A comparative study of authigenic carbonates from mussel and tubeworm environments: Implications for discriminating the effects of tubeworms. Deep Sea Res. Part I Oceanogr. 75, 110-118.

Fitriyanto, N.A., Fushimi, M., Matsunaga, M., Pertiwiningrum, A., Iwama, T., Kawai, K., 2011. Molecular structure and gene analysis of Ce^{3+}-induced methanol dehydrogenase of *Bradyrhizobium* sp. MAFF211645. J. Biosci. Bioeng. 111, 613-617.

Flores, J.F., Fisher, C.R., Carney, S.L., Green, B.N., Freytag, J.K., Schaeffer, S.W., Royer, W.E., 2005. Sulfide binding is mediated by zinc ions discovered in the crystal structure of a hydrothermal vent tubeworm hemoglobin. Proc. Nat. Acad. Sci. 102, 2713-2718.

Franchi, F., Rovere, M., Gamberi, F., Rashed, H., Vaselli, O., Tassi, F., 2017. Authigenic minerals from the Paola Ridge (southern Tyrrhenian Sea): Evidences of episodic methane seepage. Mar. Petrol. Geol. 86, 228-247.

Freytag, J.K., Girguis, P.R., Bergquist, D.C., Andras, J.P., Childress, J.J., Fisher, C.R., 2001. A paradox resolved: sulfide acquisition by roots of seep tubeworms sustains net chemoautotrophy. Proc. Nat. Acad. Sci. 98, 13408-13413.

Gaill, F., Persson, J., Sugiyama, J., Vuong, R., Chanzy, H., 1992. The chitin system in the tubes of deep-sea hydrothermal vent worms. J. Struct. Biol. 109, 116-128.

622 Gaill, F., Shillito, B., Ménard, F., Goffinet, G., Childress, J.J., 1997. Rate and process of tube
623 production by the deep-sea hydrothermal vent tubeworm Riftia pachyptila. Mar. Ecol.
624 Prog. Ser. 148, 135-143.
625 Gieskes, J., Mahn, C., Day, S., Martin, J.B., Greinert, J., Rathburn, T., McAdoo, B., 2005. A
626 study of the chemistry of pore fluids and authigenic carbonates in methane seep
627 environments: Kodiak Trench, Hydrate Ridge, Monterey Bay, and Eel River Basin. Chem.
628 Geol. 220, 329-345.
629 Glass, J.B., Orphan, V.J., 2012. Trace Metal Requirements for Microbial Enzymes Involved
630 in the Production and Consumption of Methane and Nitrous Oxide. Front. Microbiol. 3, 61.
631 doi:10.3389/fmicb.2012.00061.
632 Greinert, J., Bohrmann, G., Suess, E., 2001. Gas hydrate-associated carbonates and methane-
633 venting at Hydrate Ridge: classification, distribution and origin of authigenic lithologies.
634 Geophys. Monogr. Ser. 124, 99-114.
635 Haley, B.A., Klinkhammer, G.P., McManus, J., 2004. Rare earth elements in pore waters of
636 marine sediments. Geochim. Cosmochim. Acta 68, 1265-1279.
637 Han, X., Suess, E., Huang, Y., Wu, N., Bohrmann, G., Su, X., Eisenhauer, A., Rehder, G.,
638 Fang, Y., 2008. Jiulong methane reef: microbial mediation of seep carbonates in the South
639 China Sea. Mar. Geol. 249, 243-256.
640 Hilario, A., Capa, M., Dahlgren, T.G., Halanych, K.M., Little, C.T., Thornhill, D.J., Verna,
641 C., Glover, A.G., 2011. New perspectives on the ecology and evolution of siboglinid
642 tubeworms. PloS One 6(2).
643 Himmler, T., Bach, W., Bohrmann, G., Peckmann, J., 2010. Rare earth elements in authigenic
644 methane-seep carbonates as tracers for fluid composition during early diagenesis. Chem.
645 Geol. 277, 126-136.

646 Himmler, T., Haley, B.A., Torres, M.E., Klinkhammer, G.P., Bohrmann, G., Peckmann, J.,
647 2013. Rare earth element geochemistry in cold-seep pore waters of Hydrate Ridge,
648 northeast Pacific Ocean. Geo-Mar. Lett. 33, 369-379.
649 Himmler, T., Birgel, D., Bayon, G., Pape, T., Ge, L., Bohrmann, G., Peckmann, J., 2015.
650 Formation of seep carbonates along the Makran convergent margin, northern Arabian Sea
651 and a molecular and isotopic approach to constrain the carbon isotopic composition of
652 parent methane. Chem. Geol. 415, 102-117.
653 Hu, Y., Feng, D., Peckmann, J., Roberts, H.H., Chen, D., 2014. New insights into cerium
654 anomalies and mechanisms of trace metal enrichment in authigenic carbonate from
655 hydrocarbon seeps. Chem. Geol. 381, 55-66.
656 Hu, Y., Feng, D., Liang, Q., Xia, Z., Chen, L., Chen, D., 2015. Impact of anaerobic oxidation
657 of methane on the geochemical cycle of redox-sensitive elements at cold-seep sites of the
658 northern South China Sea. Deep-Sea Res. Part II-Top. Stud. Oceanogr. 122, 84–94.
659 International Atomic Energy Agency. MA-A-1/TM, trace elements in copepod homogenate.
660 Reference sheet. IAEA, Monaco (1990).
661 Julian, D., Gaill, F., Wood, E., Arp, A.J., Fisher, C.R., 1999. Roots as a site of hydrogen
662 sulfide uptake in the hydrocarbon seep vestimentiferan Lamellibrachia sp. J. Exp. Biol.
663 202, 2245-2257.
664 Joye, S.B., MacDonald, I.R., Leifer, I., Asper, V., 2011. Magnitude and oxidation potential of
665 hydrocarbon gases released from the BP oil well blowout. Nat. Geosci. 4, 160-164.
666 Kamber, B.S., Webb, G.E., Gallagher, M., 2014. The rare earth element signal in Archaean
667 microbial carbonate: information on ocean redox and biogenicity. J. Geol. Soc. 171, 745-
668 763.

669 Kamber, B.S., Webb, G.E., 2001. The geochemistry of late Archaean microbial carbonate:
670 implications for ocean chemistry and continental erosion history. Geochim. Cosmochim.
671 Acta 65, 2509-2525.
672 Konhauser, K.O., Pecoits, E., Lalonde, S.V., Papineau, D., Nisbet, E.G., Barley, M.E., Arndt,
673 N.T., Zahnle, K., Kamber, B.S., 2009. Oceanic nickel depletion and a methanogen famine
674 before the Great Oxidation Event. Nature 458, 750-753.
675 Lawrence, M. G., Greig, A., Collerson, K.D., Kamber, B.S., 2006. Rare earth element and
676 yttrium variability in South East Queensland waterways. Aquat. Geochem. 12, 39-72.
677 Lemaitre, N., Bayon, G., Ondréas, H., Caprais, J.C., Freslon, N., Bollinger, C., Rouget, M.L.,
678 De Prunelé, A., Ruffine, L., Olu-Le Roy, K., Sarthou, G., 2014. Trace element behaviour
679 at cold seeps and the potential export of dissolved iron to the ocean. Earth Planet. Sci. Lett.
680 404, 376-388.
681 Maher, W. Forster, S., Krikowa, F., Snitch, P., Chapple, G., Craig, P., 2001. Measurement of
682 trace elements and phosphorus in marine animal and plant tissues by low-volume
683 microwave digestion and ICP-MS. Atom. Spectroscopy 22, 361-370.
684 Marcon, Y., Ondréas, H., Sahling, H., Bohrmann, G., Olu, K., 2014. Fluid flow regimes and
685 growth of a giant pockmark. Geology 42, 63-66.
686 McManus, J., Berelson, W.M., Klinkhammer, G.P., Hammond, D.E., Holm, C., 2005.
687 Authigenic uranium: relationship to oxygen penetration depth and organic carbon rain.
688 Geochim. Cosmochim. Acta 69, 95-108.
689 Medina-Silva, R. et al., 2018. Microbiota associated with tubes of *Escarpia* sp. from cold
690 seeps in the southwestern Atlantic Ocean constitutes a community distinct from that of
691 surrounding marine sediment and water. Anton. Leeuw. Int. J. G. 111, 533-550.
692 Naehr, T. H., Eichhubl, P., Orphan, V. J., Hovland, M., Paull, C. K., Ussler III, W., Lorenson,
693 T.D., Greene, H. G., 2007. Authigenic carbonate formation at hydrocarbon seeps in

694 continental margin sediments: a comparative study. Deep-Sea Res. Part II-Top. Stud.
695 Oceanogr. 54, 1268-1291.
696 Nakagawa, T., Mitsui, R., Tani, A., Sasa, K., Tashiro, S., Iwama, T., Hayakawa, T., Kawai,
697 K., 2012. A catalytic role of XoxF1 as La^{3+}-dependent methanol dehydrogenase in
698 *Methylobacterium extorquens* strain AM1. PLoS One 7, e50480.
699 Novikova, S.A., Shnyukov, Y.F., Sokol, E.V., Kozmenko, O.A., Semenova, D.V., Kutny,
700 V.A., 2015. A methane-derived carbonate build-up at a cold seep on the Crimean slope,
701 north-western Black Sea. Mar. Geol. 363, 160-173.
702 Ochsner, A.M., Hemmerle, L., Vonderach, T., Nüssli, R., Bortfeld-Miller, M., Hattendorf, B.,
703 Vorholt, J.A., 2019. Use of rare-earth elements in the phyllosphere colonizer
704 *Methylobacterium extorquens* PA1. Mol. Microbiol. 111, 1152-1166.
705 Olu-Le Roy, K., Caprais, J. C., Fifis, A., Fabri, M. C., Galéron, J., Budzinsky, H., Le Ménach,
706 K., Khripounoff, A., Ondréas, H., Sibuet, M., 2007. Cold-seep assemblages on a giant
707 pockmark off West Africa: spatial patterns and environmental control. Mar. Ecol. 28, 115-
708 130.
709 Ondréas, H. et al., 2005. ROV study of a giant pockmark on the Gabon continental margin.
710 Geo-Mar. Lett. 25, 281-292.
711 Peketi, A., Mazumdar, A., Joshi, R.K., Patil, D.J., Srinivas, P.L., Dayal, A.M., 2012. Tracing
712 the Paleo sulfate-methane transition zones and H2S seepage events in marine sediments:
713 An application of C-S-Mo systematics. Geochem. Geophys. Geosyst. 13, Q10007,
714 doi:10.1029/2012GC004288.
715 Picone, N., Op den Camp, H.J., 2019. Role of rare earth elements in methanol oxidation.
716 Curr. Opin. Chem. Biol. 49, 39–44.
717 Pierre, C., Bayon, G., Blanc-Valleron, M.M., Mascle, J., Dupré, S., 2014. Authigenic
718 carbonates related to active seepage of methane-rich hot brines at the Cheops mud volcano,

719 Menes caldera (Nile deep-sea fan, eastern Mediterranean Sea). Geo-Mar. Lett. 34, 253-
720 267.
721 Planavsky, N., Bekker, A., Rouxel, O.J., Kamber, B., Hofmann, A., Knudsen, A., Lyons, T.
722 W., 2010. Rare earth element and yttrium compositions of Archean and Paleoproterozoic
723 Fe formations revisited: new perspectives on the significance and mechanisms of
724 deposition. Geochim. Cosmochim. Acta 74, 6387-6405.
725 Pol, A., Barends, T.R.M., Dietl, A., Khadem, A.F., Eygensteyn, J., Jetten, M.S.M., Op den
726 Camp, H.J.M., 2014. Rare earth metals are essential for methanotrophic life in volcanic
727 mudpots. Environ. Microbiol. 16, 255–264.
728 Pop Ristova, P., Wenzhofer, F., Ramette, A., Zabel, M., Fischer, D., Kasten, S., Boetius, A.,
729 2012. Bacterial diversity and biogeochemistry of different chemosynthetic habitats of the
730 REGAB cold seep (West African margin, 3160 m water depth). Biogeosciences 9, 5031-
731 5048.
732 Rincón-Tomás, B., González, F.J., Somoza, L., Sauter, K., Madureira, P., Medialdea, T.,
733 Carlsson, J., Reitner, J., Hoppert, M., 2020. Siboglinidae Tubes as an Additional Niche for
734 Microbial Communities in the Gulf of Cádiz—A Microscopical Appraisal.
735 Microorganisms 8, 367.
736 Rongemaille, E., Bayon, G., Pierre, C., Bollinger, C., Chu, N.C., Fouquet, Y., Riboulot, V.,
737 Voisset, M., 2011. Rare earth elements in cold seep carbonates from the Niger delta.
738 Chem. Geol. 286, 196–206.
739 Sato, H., Hayashi, K.I., Ogawa, Y., Kawamura, K., 2012. Geochemistry of deep sea
740 sediments at cold seep sites in the Nankai Trough: Insights into the effect of anaerobic
741 oxidation of methane. Mar. Geol. 323–325.
742 Schier, K., Bau, M., Muenker, C., Beukes, N., Viehmann, S., 2018. Trace element and Nd
743 isotope composition of shallow seawater prior to the Great Oxidation Event: Evidence

744 from stromatolitic bioherms in the Paleoproterozoic Rooinekke and Nelani Formations,
745 South Africa. Precambrian Res. 315, 92-102.
746 Schulz, H. D., Dahmke, A., Schinzel, U., Wallmann, K., Zabel, M., 1994. Early diagenetic
747 processes, fluxes, and reaction rates in sediments of the South Atlantic. Geochim.
748 Cosmochim. Acta 58, 2041-2060.
749 Semrau, J.D., DiSpirito, A.A., Gu, W., Yoon, S., 2018. Metals and methanotrophy. Appl.
750 Environ. Microbiol. 84, e02289-17.
751 Shiller, A.M., Chan, E.W., Joung, D.J., Redmond, M.C., Kessler, J.D., 2017. Light rare earth
752 element depletion during Deepwater Horizon blowout methanotrophy. Sci. Rep. 7, 10389.
753 Sholkovitz, E.R., Piepgras, D.J., Jacobsen, S.B., 1989. The pore water chemistry of rare earth
754 elements in Buzzards Bay sediments. Geochim. Cosmochim. Acta 53, 2847-2856.
755 Sibuet, M., Olu, K., 1998. Biogeography, biodiversity and fluid dependence of deep-sea cold-
756 seep communities at active and passive margins. Deep-Sea Res. Part II-Top. Stud.
757 Oceanogr. 45, 517-567.
758 Skovran, E., Martinez-Gomes, N.C., 2015. Just add lanthanides. Science 348, 862-863
759 Smrzka, D., Zwicker, J., Klügel, A., Monien, P., Bach, W., Bohrmann, G., Peckmann, J.,
760 2016. Establishing criteria to distinguish oil-seep from methane-seep carbonates. Geology
761 44, 667-670.
762 Smrzka, D., Zwicker, J., Misch, D., Walkner, C., Gier, S., Monien, P., Bohrmann, G.,
763 Peckmann, J., 2019. Oil seepage and carbonate formation: A case study from the southern
764 Gulf of Mexico. Sedimentology 66, 2318-2353.
765 Smrzka, D., Zwicker, J., Bach, W., Feng, D., Himmler, T., Chen, D., Peckmann, J., 2019. The
766 behavior of trace elements in seawater, sedimentary pore water, and their incorporation
767 into carbonate minerals: a review. Facies 65, 41.

768 Smrzka, D., Feng, D., Himmler, T., Zwicker, J., Hu, Y., Monien, P., Tribovillard, N., Chen,
769 D., Peckmann, J., 2020. Trace elements in methane-seep carbonates: Potentials,
770 limitations, and perspectives. Earth Sci. Rev. 208, 103263.
771 Taubert, M., Grob, C., Howat, A.M., Burns, O.J., Dixon, J.L., Chen, Y., Murrell, J.C., 2015.
772 XoxF encoding an alternative methanol dehydrogenase is widespread in coastal marine
773 environments. Environ. Microbiol. 17, 3937-3948.
774 Teichert, B. M., Bohrmann, G., Suess, E., 2005. Chemoherms on Hydrate Ridge—Unique
775 microbially-mediated carbonate build-ups growing into the water column. Palaeogeog.
776 Palaeoclimatol. Palaeoecol. 227, 67-85.
777 Tong, H., Chen, D., 2012. First discovery and characterizations of late Cretaceous seep
778 carbonates from Xigaze in Tibet, China. Chin. Sci. Bull. 57, 4363-4372.
779 Tribovillard, N., Algeo, T.J., Lyons, T., Riboulleau, A., 2006. Trace metals as paleoredox and
780 paleoproductivity proxies: an update. Chem. Geol. 232, 12-32.
781 Tribovillard, N., Du Châtelet, E.A., Gay, A., Barbecot, F., Sansjofre, P., Potdevin, J.L., 2013.
782 Geochemistry of cold seepage-impacted sediments: per-ascensum or per-descensum trace
783 metal enrichment?. Chem. Geol. 340, 1-12.
784 Tyler, G., 2004. Rare earth elements in soil and plant systems – A review. Plant Soil 267,
785 191-206.
786 Wang, S., Magalhães, V.H., Pinheiro, L.M., Liu, J., Yan, W., 2015. Tracing the composition,
787 fluid source and formation conditions of the methane-derived authigenic carbonates in the
788 Gulf of Cadiz with rare earth elements and stable isotopes. Mar. Petrol. Geol. 68, 192-205.
789 Wang, S., Yan, W., Chen, Z., Zhang, N., Chen, H., 2014. Rare earth elements in cold seep
790 carbonates from the southwestern Dongsha area, northern South China Sea. Mar. Petrol.
791 Geol. 57, 482-493.

Wang, X., Bayon, G., Kim, J.H., Lee, D.H., Kim, D., Guéguen, B., Rouget, M.L., Barrat, J.A., Toffin, L., Feng, D., 2019. Trace element systematics in cold seep carbonates and associated lipid compounds. Chem. Geol. 528, 119277.

Wang, X., Barrat, J.A., Bayon, G., Chauvaud, L., Feng, D., 2020. Lanthanum anomalies as fingerprints of methanotrophy. Geochem. Perspect. Lett. (in press).

Yang, K., Chu, F., Zhu, Z., Dong, Y., Yu, X., Zhang, W., Ma, W., 2018. Formation of methane-derived carbonates during the last glacial period on the northern slope of the South China Sea. J. Asian Earth Sci. 168, 173-185.

Zhu, B., Ge, L., Yang, T., Jiang, S., Lv, X., 2019. Stable isotopes and rare earth element compositions of ancient cold seep carbonates from Enza River, northern Apennines (Italy): Implications for fluids sources and carbonate chimney growth. Mar. Petrol. Geol. 109, 434-448.

Zwicker, J., Smrzka, D., Himmler, T., Monien, P., Gier, S., Goedert, J.L., Peckmann, J., 2018. Rare earth elements as tracers for microbial activity and early diagenesis: A new perspective from carbonate cements of ancient methane-seep deposits. Chem. Geol. 501, 77-85.

Figure captions

Figure 1. **(a)** Seafloor photographs of bushes of siboglinid tubeworms (*Escarpia southwardae*) at the Regab pockmark. **(b)** The chitin-rich tube of *Escarpia southwardae* investigated in this study, with location of the sections analysed for trace elements.

Figure 2. Concentration profiles for selected trace elements (µg/g or ng/g), La and Ce anomalies, and shale-normalized La/Gd ratios along the tube. The anterior part of the tube

817 (from sections S1 to S8) corresponds to a redox front between ambient oxic seawater and the
818 branchial plume region, characterized by oxygen-depleted conditions (horizontal orange
819 band). The part of the tube between sections S1 and S44 was bathed by bottom water, while
820 sections S44 to S55 correspond to the root-like posterior extension buried in the anoxic
821 sediment. The second redox front between sections S44 to S49 corresponds to the seawater-
822 sediment interface (horizontal orange band). The vertical grey shaded areas indicate the range
823 of $(La/Gd)_N$, La and Ce anomalies in bottom waters at Regab (Lemaitre et al., 2014). The
824 dashed lines correspond to La/La* and Ce/Ce* = 1, which indicate the absence of any La and
825 Ce anomalies, respectively. Note that Mn and Fe concentrations are from Duperron et al.
826 (2014).
827
828 **Figure 3**. Shale-normalized (WRAS) REE patterns for the studied siboglinid tube between (**a**)
829 sections S1 and S8, (**b**) sections S9-S21, and (**c**) sections S22-S44 and S45-S55. (**d**) Also
830 shown for comparison are the average REE patterns for Regab bottom waters (Lemaitre et al.,
831 2014), together with global seawater and pore waters having shale-normalized Gd/Yb ratio >1
832 (considered as representative of anoxic pore waters). The references used for the global
833 compilation of seawater and pore water data are listed in Supplementary Tables S1 and S2.
834 Note that the tube samples from sections S22-S44 (black circles) and S45-S55 (blue squares)
835 display REE patterns typical ambient bottom waters at the Regab pockmark and anoxic pore
836 waters, respectively. In contrast, samples from sections S8-S21 (orange triangles) and S3-S7
837 (red diamonds) are characterized by pronounced La enrichments and the absence of Ce
838 anomalies. The observed flat shale-normalized patterns for sections S1 and S2 reflect the
839 presence of detrital sediment particles.
840

841 **Figure 4**. Relationship between Ce and La anomalies in studied siboglinid tube sections. The
842 other REE data used for comparison include a global compilation of Ce/Ce* and La/La* for
843 seawater and pore water (Tables S1 and S2), bottom waters at the Regab pockmark (Lemaitre
844 et al., 2014) collected just above the seafloor (<1 m absf) and in the overlying water column
845 (>1 m absf) (Lemaitre et al., 2014), and the Fe-Mn oxyhydroxide fraction extracted from
846 Congo fan seafloor sediment (yellow star; Bayon et al., 2004). The tube sections from the
847 buried posterior extension between sections S45-S55 plot within the field of pore waters
848 (expect for S51 and S52), while the sections S22-S44 plot between the fields for pore waters
849 and ambient bottom waters at Regab. In contrast, most of the sections from the anterior part of
850 the tube display clear La enrichments that depart from expected pore water and seawater
851 signatures.
852
853 **Figure 5**. Relationships between light-REE and Cu in the siboglinid tube sections. (**a**) La/Th
854 vs Cu/Th. (**b**) La/La* vs Cu/Th. (**c**) Ce/Th vs Cu/Th. (**d**) Ce/Ce* vs Cu/Th. The observed co-
855 enrichments of Cu, La and (to a lesser extent) Ce and in the anterior portion of the tube are
856 interpreted as reflecting their uptake by aerobic methane-oxidising bacteria, as
857 metalloenzymes catalyzing the transformation of methane to methanol, and methanol to
858 formaldehyde, respectively.
859
860 **Figure 6**. Revisiting REE systematics in modern cold seep carbonates using (**a**) Ce/Ce* vs
861 La/La* and (**b**) $(La/Gd)_N$ vs $(Gd/Yb)_N$ relationships. The REE data and references used for the
862 compilation of cold seep carbonates are listed in Table S3. Most cold seep carbonates overlap
863 with pore waters, except for some seafloor aragonite-rich chemoherms displaying particular
864 La enrichments, as inferred from high $(La/Gd)_N$ (> ~ 0.8). These LREE enrichments are
865 interpreted here as possibly reflecting the signature of REE-dependent methanotrophic

activity at the seafloor. Also shown for comparison are average laser-ablation data for pure aragonite in seep carbonates from the Makran accretionary prism (Himmler et al., 2010), in seep carbonates influenced by oil seepage in the Gulf of Mexico (Smrzka et al., 2019), and in ancient Phanerozoic seep carbonates (Zwicker et al., 2018).

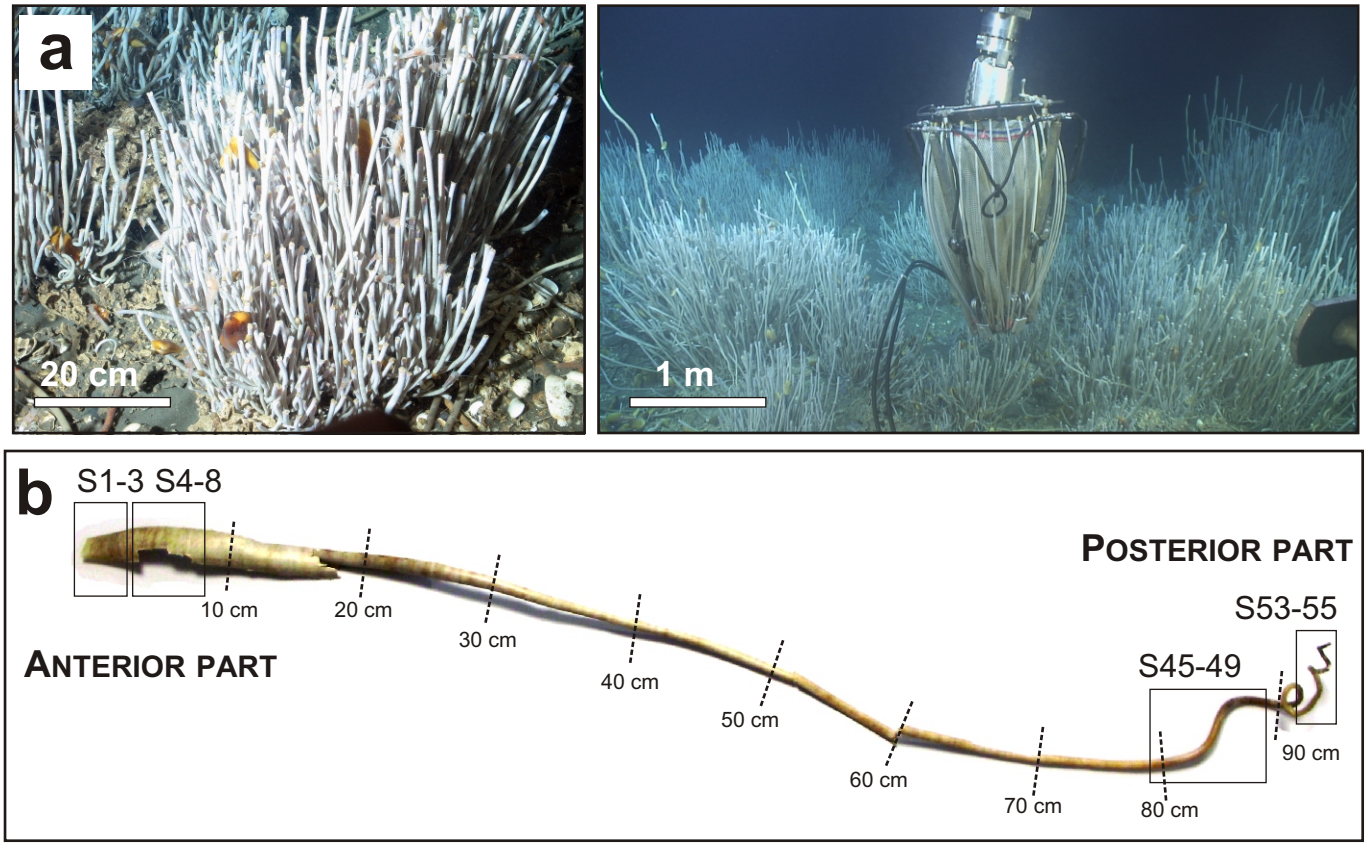
a
20 cm
1 m
b
S1-3 S4-8
10 cm
20 cm
30 cm
40 cm
50 cm
60 cm
70 cm
80 cm
90 cm
ANTERIOR PART
POSTERIOR PART
S45-49
S53-55

Fig. 1

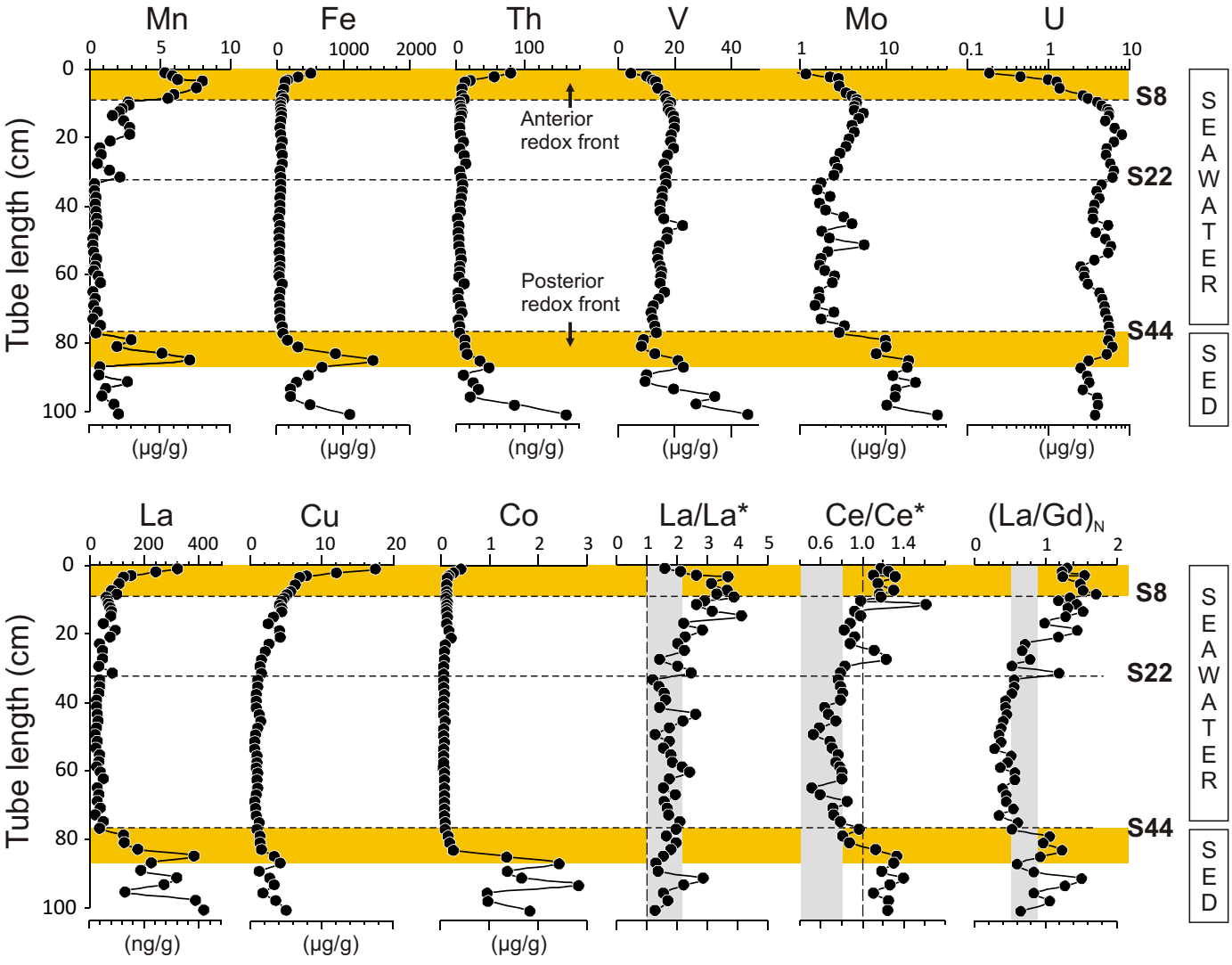
Mn
Fe
Th
V
Mo
U
Tube length (cm)
Anterior redox front
Posterior redox front
S8
S22
S44
SEAWATER
SED
(µg/g)
(ng/g)
La
Cu
Co
La/La*
Ce/Ce*
(La/Gd)N

Fig. 2

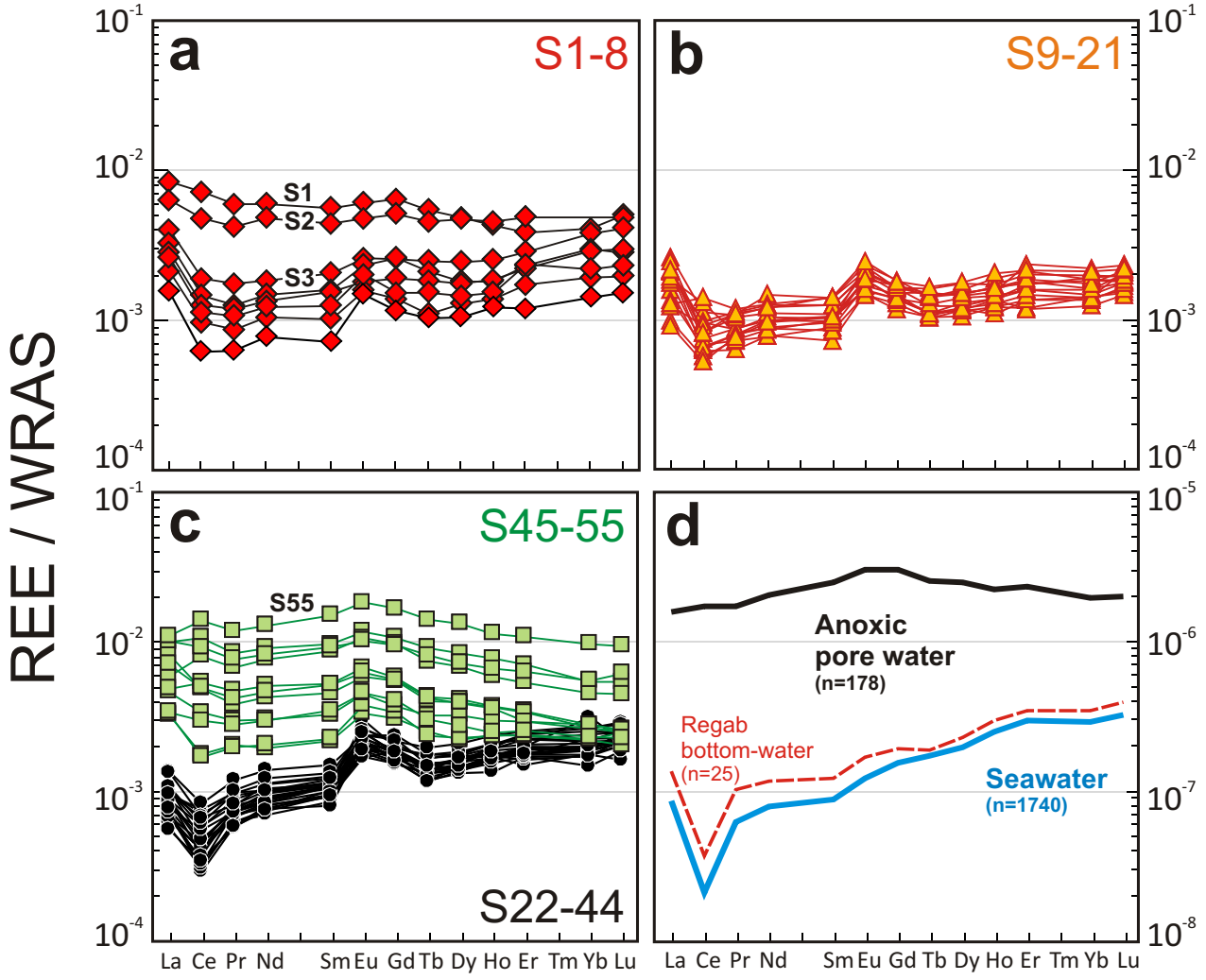
REE / WRAS
a
S1-8
S1
S2
S3
b
S9-21
c
S45-55
S55
S22-44
d
Anoxic
pore water
(n=178)
Regab
bottom-water
(n=25)
Seawater
(n=1740)
La Ce Pr Nd Sm Eu Gd Tb Dy Ho Er Tm Yb Lu

Fig. 3

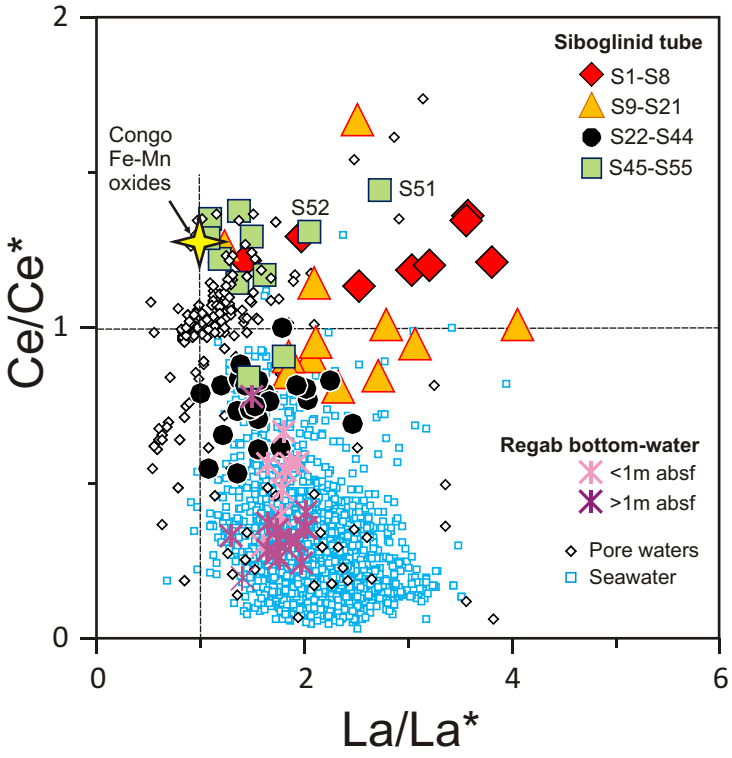
Siboglinid tube
S1-S8
S9-S21
S22-S44
S45-S55
Congo
Fe-Mn
oxides
S52
S51
Regab bottom-water
<1m absf
>1m absf
Pore waters
Seawater
Ce/Ce*
La/La*
0
1
2
0
2
4
6

Fig. 4

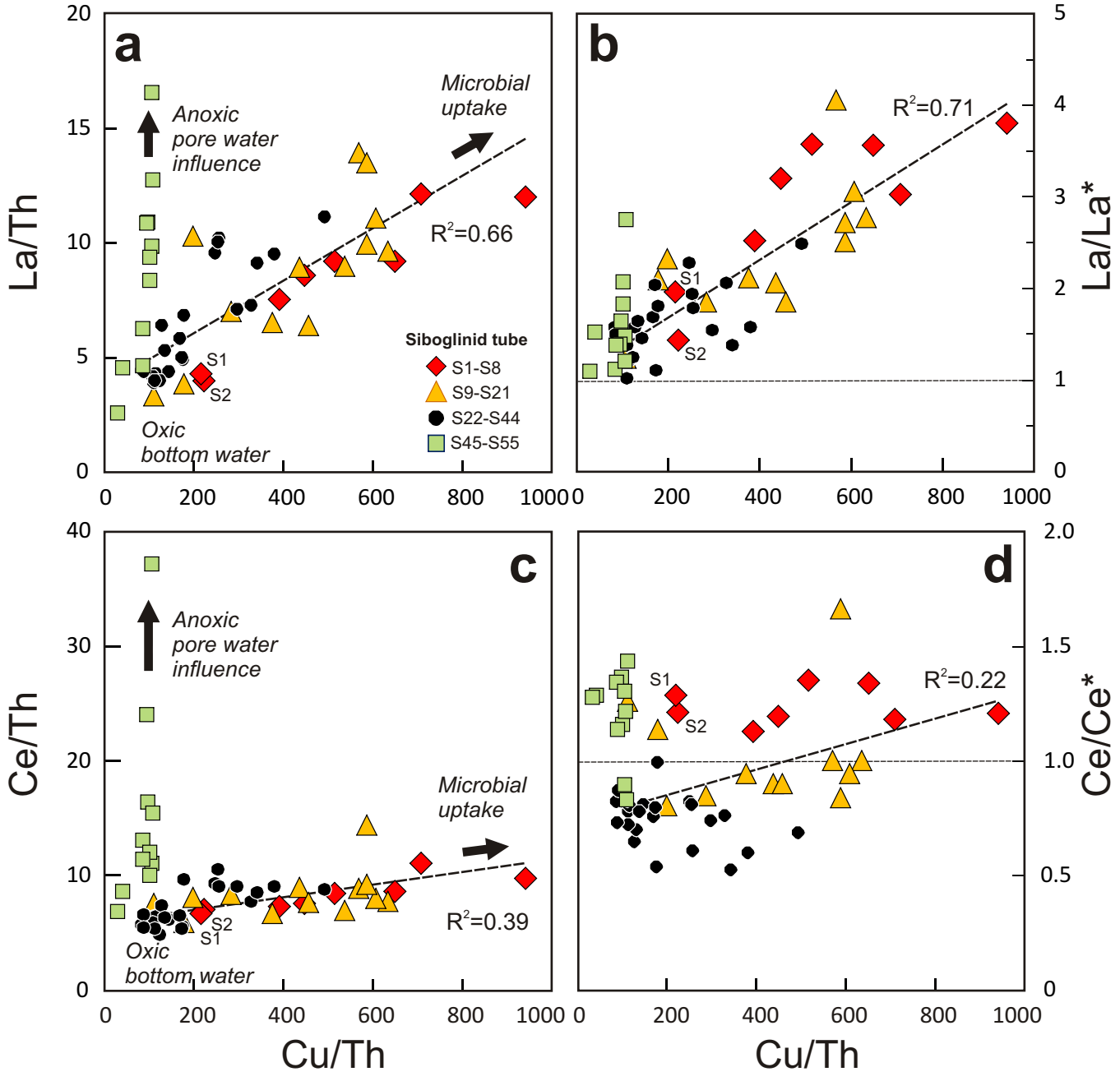
a
b
c
d
Anoxic
pore water
influence
Microbial
uptake
Oxic
bottom water
R²=0.66
R²=0.71
R²=0.39
R²=0.22
S1
S2
Siboglinid tube
S1-S8
S9-S21
S22-S44
S45-S55
La/Th
La/La*
Ce/Th
Ce/Ce*
Cu/Th
Cu/Th

Fig. 5

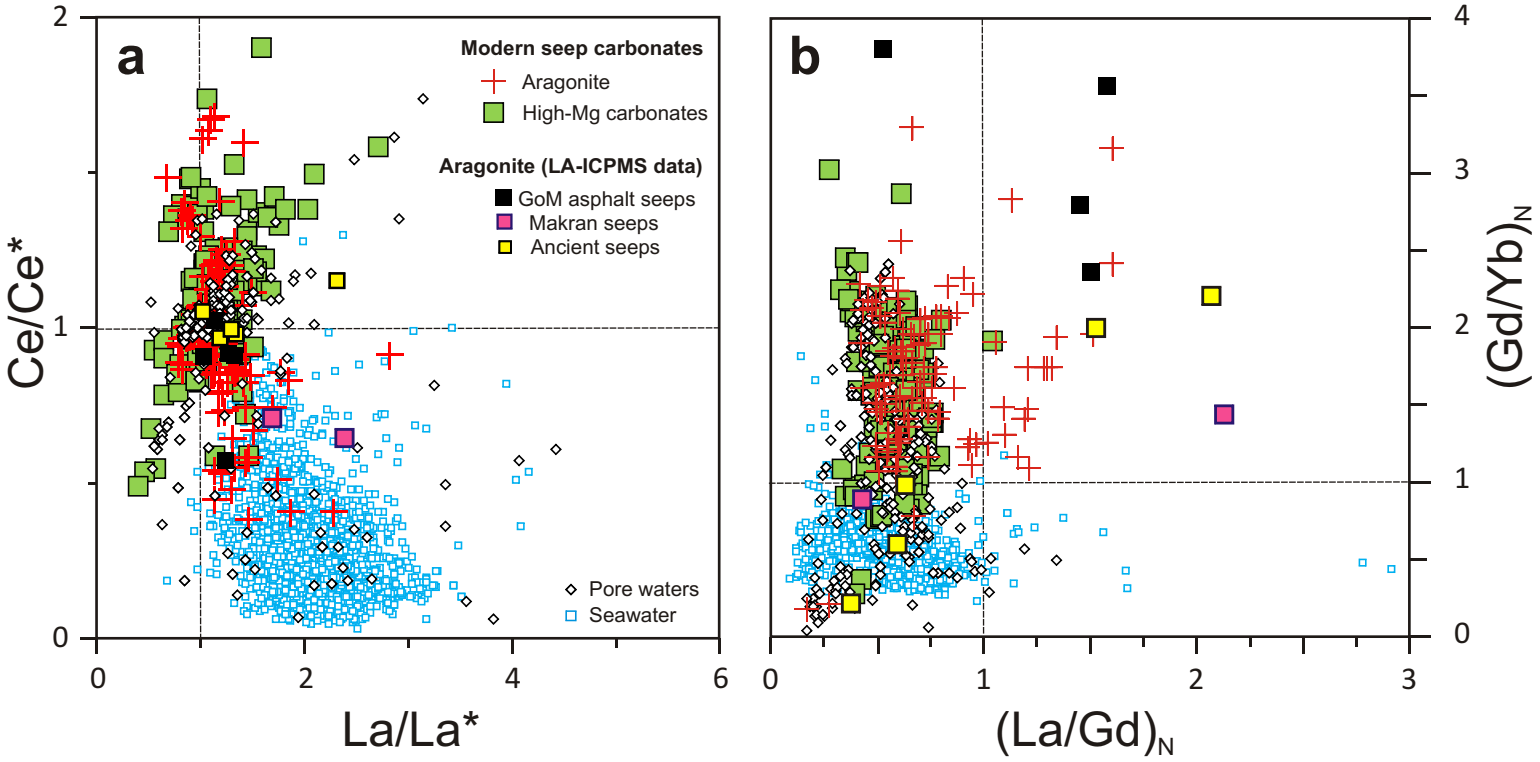
a
Modern seep carbonates
Aragonite
High-Mg carbonates
Aragonite (LA-ICPMS data)
GoM asphalt seeps
Makran seeps
Ancient seeps
Pore waters
Seawater
Ce/Ce*
La/La*
b
(La/Gd)N
(Gd/Yb)N

Fig. 6

Table 1. Trace element concentrations for MA-A-1 (Copepod Homogenate)

Element	Mean concentration (n=4)	s	RSD (%)	After Fe-ox coprecipitation (n=1)	Certified values (IAEA, 1990)	Other reference values (Maher et al., 2001)
µg/g						
V	3.29	0.16	4.7			4.1
Mn	2.94	0.30	10.3	2.90	2.8	2.8
Fe	60.7	3.0	5.0		58	64
Co	0.122	0.009	7.5		0.14	0.13
Ni	1.52	0.12	8.1		1.62	1.83
Cu	6.71	0.17	2.6		7.51	7.05
Zn	166	12	7.5		160	155
Rb	2.48	0.14	5.6			
Sr	53.4	1.3	2.5			
Zr	0.05	0.01	18.7			
Mo	0.26	0.06	24.0			
Ba	1.00	0.07	7.3			
U	0.83	0.04	5.2			
ng/g						
Y	19.3	1.4	7.0	18.5		
La	30.1	2.5	8.3	30.6		
Ce	48.3	2.2	4.6	49.3		
Pr	5.6	0.4	7.2	5.8		
Nd	21.8	1.1	4.9	21.5		
Sm	4.1	0.3	6.2	4.2		
Eu	0.64	0.08	12.3	0.96		
Gd	3.16	0.57	18.1	2.72		
Tb	0.48	0.04	8.8	0.65		
Dy	2.81	0.25	8.8	2.86		
Ho	0.52	0.08	14.8	0.57		
Er	1.61	0.15	9.3	1.46		
Yb	1.26	0.10	8.3	1.26		
Lu	0.17	0.02	13.1			
Th	3.29	0.52	15.8	3.44		

Table 2. Trace element concentrations for the tube sections

N°	Length (cm)	V (µg/g)	Mn (µg/g)	Fe (µg/g)	Co (µg/g)	Ni (µg/g)	Cu (µg/g)	Zn (µg/g)	Rb (µg/g)	Sr (µg/g)	Zr (µg/g)	Mo (µg/g)	Ba (µg/g)	U (µg/g)	Th (ng/g)
S1	1	4.3	5.33	513	0.42	43.6	17.6	41.3	0.73	30.0	0.40	0.65	8.01	0.19	79.0
S2	2	9.8	5.88	322	0.26	47.3	12.1	15.3	0.53	21.4	0.44	1.24	2.65	0.48	55.8
S3	3	12.1	6.24	162	0.17	33.4	7.9	10.5	0.37	17.2	0.34	2.40	1.72	1.08	20.1
S4	3.5	13.2	7.95	123	0.14	30.8	6.9	12.4	0.34	14.9	0.19	2.96	1.57	1.39	13.4
S5	5.5	13.9	7.57	104	0.12	28.5	6.3	9.2	0.32	13.8	0.24	3.07	0.87	1.54	8.9
S6	7.5	16.4	5.94	75	0.12	30.3	5.6	9.7	0.16	10.6	0.22	3.64	0.53	3.04	8.7
S7	8.5	16.7	5.52	104	0.13	29.2	5.2	8.1	0.29	12.4	0.22	4.33	0.79	3.53	11.5
S8	9.5	18.5	2.73	59	0.11	28.1	4.7	8.6	0.18	13.2	0.17	4.95	0.52	4.59	5.0
S9	10.5	17.6	2.80	64	0.14	30.0	4.4	5.9	0.18	11.5	0.16	4.88	0.52	5.20	6.9
S10	11.5	17.6	2.30	62	0.13	30.3	4.1	8.9	0.21	11.0	0.16	4.62	0.67	6.26	7.0
S11	12.5	18.3	2.10	75	0.12	29.8	4.5	7.0	0.22	13.1	0.18	4.60	0.71	6.46	8.3
S12	13.5	19.3	1.61	71	0.13	30.0	4.4	7.7	0.21	11.5	0.14	5.91	1.41	6.50	7.3
S13	15	19.6	2.40	55	0.14	22.7	3.2	7.5	0.25	14.4	0.16	5.28	0.90	5.91	5.7
S14	17	19.6	2.83	52	0.13	17.9	2.5	5.2	0.17	12.7	0.14	4.34	0.40	7.76	5.7
S15	19	18.6	2.83	63	0.17	32.0	4.1	7.9	0.18	14.3	0.19	4.63	0.49	9.64	6.9
S16	21	18.4	1.48	85	0.21	34.6	4.2	6.7	0.19	12.6	0.17	4.00	1.44	7.60	11.2
S17	23	19.4	0.73	58	0.09	19.8	2.6	5.5	0.17	14.4	0.14	3.69	0.37	6.07	5.8
S18	25	17.3	0.83	77	0.07	15.7	2.1	6.9	0.16	12.4	0.16	3.13	0.54	5.96	12.1
S19	27.5	15.9	0.57	79	0.07	12.5	1.6	11.2	0.16	11.3	0.16	2.72	0.63	6.76	14.4
S20	29.5	17.1	1.40	45	0.06	11.8	1.4	5.6	0.17	13.6	0.13	2.91	0.28	7.52	4.9
S21	31.5	16.6	2.15	56	0.07	12.6	1.6	10.5	0.17	14.0	0.15	2.67	0.49	7.24	7.9
S22	33.5	16.6	0.35	61	0.07	10.1	1.0	7.6	0.17	11.2	0.11	1.86	0.56	5.31	9.3
S23	35.5	15.4	0.34	57	0.07	9.9	1.0	7.0	0.20	11.6	0.14	1.69	0.49	4.51	8.7
S24	37.5	15.4	0.44	53	0.08	10.2	0.9	6.7	0.17	12.2	0.12	2.39	0.45	4.96	7.9
S25	39.5	14.8	0.38	45	0.06	9.5	0.9	7.7	0.14	10.5	0.11	1.78	0.38	4.21	5.8
S26	41.5	14.7	0.43	53	0.06	9.3	0.8	11.1	0.12	10.9	0.09	2.09	0.38	4.06	6.5
S27	43.5	16.0	0.50	32	0.06	12.0	1.3	8.9	0.16	13.9	0.11	3.48	0.36	4.06	2.6
S28	45.5	22.5	0.55	49	0.09	11.7	1.5	7.9	0.17	16.2	0.17	4.32	0.60	6.40	4.5
S29	47.5	17.4	0.42	42	0.06	10.7	1.0	16.2	0.17	13.5	0.11	1.88	0.43	4.45	2.7
S30	49.5	17.1	0.23	36	0.06	10.6	0.8	8.9	0.18	12.2	0.12	2.33	0.30	5.79	4.4
S31	51.5	14.3	0.26	44	0.07	10.6	0.6	11.7	0.17	12.5	0.18	6.00	0.35	6.98	4.5
S32	53.5	13.9	0.27	42	0.07	11.2	0.7	21.2	0.20	12.5	0.14	2.25	0.48	6.43	6.0
S33	55.5	13.9	0.53	51	0.07	11.3	1.0	11.8	0.23	12.3	0.13	1.85	0.61	4.24	7.1
S34	57.5	14.6	0.38	45	0.06	11.1	1.0	10.8	0.27	14.2	0.12	1.79	0.44	2.86	5.7
S35	59	15.3	0.28	35	0.06	10.9	0.9	5.6	0.23	12.6	0.08	2.08	0.28	3.18	5.1
S36	60.5	14.9	0.61	42	0.07	12.4	1.0	7.2	0.25	13.5	0.12	2.69	0.38	3.17	4.0
S37	62.5	14.7	0.79	87	0.08	21.2	1.0	9.7	0.21	11.6	0.18	2.51	2.85	3.52	11.6
S38	65	16.1	0.25	44	0.08	11.8	1.0	8.3	0.22	13.2	0.12	1.73	0.33	4.94	3.0
S39	67	14.2	0.37	40	0.09	10.7	0.8	11.4	0.24	12.7	0.15	1.77	0.28	5.42	3.2
S40	69	12.3	0.29	49	0.07	9.7	0.6	6.2	0.23	10.6	0.11	1.57	0.33	5.76	6.6
S41	71	11.6	0.57	48	0.07	9.8	0.8	6.8	0.23	11.1	0.11	2.62	0.38	5.87	8.8
S42	73	11.9	0.25	48	0.08	10.6	0.9	10.8	0.22	11.5	0.12	1.86	0.24	6.33	3.0
S43	75	12.9	0.78	82	0.10	11.9	1.3	9.5	0.26	13.1	0.21	3.50	0.27	6.48	5.1
S44	77	13.3	0.43	97	0.10	13.4	1.0	22.7	0.19	12.5	0.23	3.02	0.38	6.72	5.4
S45	79	8.9	2.93	156	0.16	13.0	1.4	13.9	0.22	11.7	0.23	10.7	0.67	6.37	12.6
S46	81	7.9	1.95	315	0.18	14.2	1.4	10.4	0.23	12.1	0.23	11.0	0.56	7.19	13.5
S47	83	12.7	5.10	881	0.26	16.0	1.6	8.7	0.29	13.7	0.18	8.51	0.93	6.16	16.2
S48	85	21.1	7.07	1431	1.36	38.4	3.4	22.8	0.34	18.9	0.40	20.6	3.44	3.61	35.0
S49	87	22.8	0.70	679	2.44	63.8	4.2	25.0	0.30	15.0	0.52	19.7	2.87	2.81	48.4
S50	89.3	9.9	0.66	477	1.37	34.4	1.2	17.7	0.22	12.0	0.29	13.3	1.41	3.45	11.3
S51	91.3	9.3	2.66	292	1.67	35.4	2.7	27.5	0.33	14.6	0.35	24.6	2.28	3.68	24.8
S52	93.3	19.5	1.13	205	2.84	50.6	3.4	24.1	0.30	14.6	0.40	14.4	4.03	3.01	32.5
S53	95.6	34.0	0.88	203	0.96	19.3	1.8	35.3	0.27	13.3	0.44	14.2	2.89	4.60	20.7
S54	97.9	27.4	1.73	502	0.98	27.1	3.6	22.0	0.43	28.6	0.74	11.2	15.5	4.70	84.7
S55	100.8	45.7	2.03	1084	1.84	36.9	5.1	23.0	0.47	21.7	1.29	45.2	19.6	4.32	160

Table 2. (continued))

N°	Y (ng/g)	La (ng/g)	Ce (ng/g)	Pr (ng/g)	Nd (ng/g)	Sm (ng/g)	Eu (ng/g)	Gd (ng/g)	Tb (ng/g)	Dy (ng/g)	Ho (ng/g)	Er (ng/g)	Yb (ng/g)	Lu (ng/g)
S1	132	319	561	52.4	197	34.9	7.25	33.5	4.50	24.1	4.43	11.6	12.4	2.32
S2	135	242	372	37.1	158	27.4	5.72	26.7	3.74	23.6	4.67	14.6	23.3	2.23
S3	80	152	148	15.5	61	12.8	3.09	13.4	2.05	12.2	2.59	8.57	11.5	1.89
S4	64	124	114	11.1	49	9.9	2.81	13.7	1.75	9.1	1.87	6.94	9.05	1.29
S5	63	109	98	10.5	44	9.6	2.16	10.0	1.52	8.7	1.92	6.63	8.76	1.37
S6	47	80	75	7.6	34	6.3	1.89	7.2	0.91	6.4	1.42	5.15	5.83	0.91
S7	59	100	88	9.5	40	7.7	2.41	8.0	1.26	7.2	1.57	7.03	6.67	1.07
S8	44	60	49	5.6	26	4.5	1.79	6.1	0.86	5.2	1.26	3.59	4.35	0.70
S9	44	67	53	6.4	26	5.5	2.02	7.7	0.89	5.8	1.12	4.06	4.35	0.97
S10	43	70	102	7.3	29	5.2	1.76	6.7	0.85	5.8	1.40	3.52	3.77	0.67
S11	49	75	58	7.6	126	6.2	1.96	7.8	0.47	5.8	1.27	3.82	4.04	0.77
S12	47	81	58	7.8	33	6.6	1.91	7.3	0.93	5.7	1.24	4.07	4.11	0.77
S13	56	79	50	7.0	33	6.1	2.72	8.4	1.02	6.2	1.42	4.74	4.48	0.82
S14	54	51	51	7.1	29	5.9	2.23	7.1	0.91	6.0	1.32	4.37	4.23	0.73
S15	63	94	64	9.2	37	6.8	2.45	8.8	1.23	7.3	1.71	5.26	5.55	0.83
S16	63	74	76	10.0	41	7.8	2.45	8.6	1.19	7.6	1.65	5.40	4.93	0.81
S17	59	37	44	6.5	28	6.2	2.23	7.2	1.06	7.0	1.49	4.76	4.83	0.95
S18	109	47	72	9.6	48	8.7	2.76	9.5	1.17	7.9	1.93	6.27	5.67	0.85
S19	102	49	110	10.5	42	8.7	2.53	8.5	1.34	8.7	1.76	5.98	6.00	0.90
S20	65	34	41	6.8	32	6.5	2.23	8.9	1.18	7.5	1.68	5.57	5.30	0.99
S21	79	82	64	9.8	40	8.8	2.93	9.4	1.37	8.9	2.10	6.44	6.39	1.00
S22	65	36	59	8.7	33	7.1	2.55	8.8	1.27	7.0	1.74	5.29	5.33	0.74
S23	67	38	55	8.3	33	6.7	2.34	9.2	1.18	7.3	1.69	5.30	5.68	0.96
S24	68	33	46	7.1	30	6.5	2.62	8.5	1.28	7.8	1.73	6.01	9.53	1.00
S25	62	26	36	6.0	27	5.7	2.19	8.0	1.09	6.8	1.73	4.48	5.47	0.93
S26	65	26	31	6.1	26	5.8	2.03	8.0	1.08	7.2	1.77	4.89	5.26	0.93
S27	72	29	23	5.1	26	5.9	2.30	8.7	1.13	7.3	1.77	5.76	5.90	1.03
S28	91	33	34	7.1	37	7.6	3.17	10.8	1.37	9.1	2.11	7.17	7.73	1.15
S29	73	26	25	5.5	25	6.3	2.23	9.5	1.15	7.6	1.94	5.88	5.77	1.12
S30	71	21	24	5.6	23	5.3	2.58	8.4	0.96	6.8	1.67	5.66	5.66	0.99
S31	79	29	33	6.5	30	6.7	3.58	10.3	1.38	8.6	2.03	7.37	8.09	1.33
S32	71	24	32	6.1	28	6.7	2.82	11.6	1.24	7.8	1.98	6.71	7.34	1.14
S33	64	38	45	7.8	35	6.9	2.45	10.1	1.14	8.5	1.88	5.38	5.93	1.04
S34	66	33	37	6.5	29	6.8	2.02	9.8	1.10	7.2	1.71	5.46	5.73	1.14
S35	60	25	27	5.1	25	4.9	2.59	9.4	0.98	6.6	1.39	5.09	4.48	0.86
S36	66	38	37	6.6	32	7.0	2.74	9.3	1.24	8.2	1.78	5.75	6.03	0.97
S37	76	51	65	10.5	46	9.3	2.86	12.4	1.44	8.7	2.16	6.76	6.67	1.17
S38	74	27	25	6.5	29	6.7	2.96	9.3	1.18	7.0	1.78	5.95	6.00	1.00
S39	71	33	29	6.8	32	6.8	2.46	9.9	1.21	8.1	2.03	6.16	6.38	0.96
S40	60	29	43	6.4	28	6.2	2.46	8.9	1.04	6.9	1.61	5.12	5.19	1.04
S41	90	41	48	8.6	37	7.8	2.66	10.1	1.45	9.1	2.14	6.67	6.60	1.00
S42	60	21	26	5.2	25	5.8	2.25	8.3	0.96	7.3	1.68	5.89	6.09	0.99
S43	78	51	53	8.9	40	8.2	3.11	11.3	1.62	10.4	2.42	7.60	8.29	1.28
S44	58	37	52	7.3	33	7.5	2.95	9.5	1.21	8.3	1.87	5.27	6.85	1.04
S45	83	125	139	18	64	13.5	4.02	16.1	2.08	11.0	2.46	7.07	6.75	0.94
S46	80	126	134	18	68	14.1	4.54	17.8	1.96	11.4	2.41	7.16	6.84	1.14
S47	103	177	265	26	100	20.2	5.39	19.6	2.66	16.2	3.06	8.86	7.95	1.20
S48	240	379	838	75	302	60.1	14.0	56.0	7.57	41.8	7.95	21.2	16.6	2.49
S49	160	225	633	60	254	53.8	12.7	51.0	6.10	34.0	6.07	16.0	13.8	2.06
S50	109	187	419	42	168	32.4	8.03	30.4	3.55	20.6	3.81	10.4	8.48	1.17
S51	108	317	383	34	141	28.3	7.05	28.8	3.35	19.7	3.79	10.1	8.19	1.13
S52	103	272	390	37	153	32.1	7.51	29.1	3.50	19.5	3.68	8.80	8.48	1.19
S53	78	129	234	25	98	21.6	5.51	21.3	2.50	13.8	2.55	7.60	7.06	1.05
S54	184	385	722	68	272	57.4	12.2	49.6	6.71	35.9	6.79	19.0	16.9	2.85
S55	299	417	1093	105	425	93.5	22.0	87.3	11.6	66.4	11.7	32.4	29.7	4.33